AIP | Physics of Fluids

An investigation of mixing in a three-stream turbulent jet

David H. Rowinski and Stephen B. Pope

Citation: Phys. Fluids **25**, 105105 (2013); doi: 10.1063/1.4822434
View online: http://dx.doi.org/10.1063/1.4822434
View Table of Contents: http://pof.aip.org/resource/1/PHFLE6/v25/i10
Published by the AIP Publishing LLC.

PHYSICS OF FLUIDS **25**, 105105 (2013)

An investigation of mixing in a three-stream turbulent jet

David H. Rowinski[a] and Stephen B. Pope
Sibley School of Mechanical and Aerospace Engineering, Cornell University,
Ithaca, New York 14850, USA

(Received 3 January 2013; accepted 26 August 2013; published online 10 October 2013)

Mixing models are required to account for the effects of molecular diffusion in probability density function (PDF) methods for reacting flows, and these models entail one of the greatest sources of modeling uncertainty in PDF calculations. In this work, we perform PDF calculations of a turbulent coaxial jet using both Reynolds-Averaged Navier-Stokes (RANS) and Large Eddy Simulation (LES) based methods. The configuration of the coaxial jet comes from a recently developed experiment, in which the conditional diffusion and scalar dissipation rate of two conserved scalars are measured. These measurements present the unique opportunity to compare directly the conditional diffusion implied by PDF mixing models to the measured conditional diffusion. In the RANS-PDF calculations, three classic mixing models are evaluated: Interaction by Exchange with the Mean (IEM), Modified Curl (MC), and Euclidean Minimum Spanning Tree (EMST). Though calculations with all three mixing models yield time-averaged mean and RMS statistics of the two scalars in good agreement with the experimental measurements, the joint PDFs of the two scalars show a wide variability from the measurements. The EMST mixing model is unique in that it produces compositions which lie very close to the slow manifold identified in the experimental work. Next, LES calculations of the same flow are performed, and the dissipation rate and conditional diffusion are calculated. The resolved scalar dissipation rate is found to be in good agreement with the experimental data, but depends strongly on the resolution; the total dissipation rate from the RANS-PDF and LES calculations indicates significantly larger scalar dissipation rates than those measured experimentally. Finally, LES-PDF calculations of the same flow yield joint PDFs in very good agreement with the experimental data. The *attenuation of variance production* model is introduced and tested in this flow: this new model is found to yield calculations of improved accuracy in LES-PDF calculations on coarse grids. © *2013 AIP Publishing LLC*. [http://dx.doi.org/10.1063/1.4822434]

I. INTRODUCTION

The probability density function (PDF) method[1,2] is a useful tool for modeling turbulent reacting flows because the chemical source term is closed, and therefore, can be treated without any additional modeling. Because of this ability to account for the highly nonlinear chemical source term, the PDF method has yielded successful calculations of turbulent flames, including those which exhibit turbulence-chemistry interactions such as extinction and re-ignition.[3–7] However, the PDF method depends on mixing models to account for the effects of molecular diffusion. Chemical reaction and molecular diffusion are inherently highly coupled physical processes, so the mixing models incur one of the largest sources of modeling uncertainty in PDF calculations. Therefore, in order to develop sound computational methodologies based on the PDF method, it is essential to have a good understanding of (i) the fundamental mixing process, (ii) the ability of mixing models to represent this process, and (iii) the sensitivity of calculations to the mixing models.

---

[a] Electronic mail: dhr46@cornell.edu

In PDF methods, a transport equation for the PDF of composition or the joint PDF of velocity, turbulence frequency, and composition is solved. For example, in the composition PDF method for constant-property flow, the PDF transport equation is

$$\frac{\partial f_\phi}{\partial t} + \frac{\partial}{\partial x_j}\left(f_\phi\left(U_j + \langle u_j|\psi\rangle\right)\right) = -\frac{\partial}{\partial \psi}\left(f_\phi\left(\langle \Gamma\nabla^2\phi|\psi\rangle + S(\psi)\right)\right), \tag{1}$$

where f_ϕ is the PDF of the composition, ϕ, U_j, and u_j are the mean and fluctuating velocities, S is the reaction source term, Γ is the molecular diffusivity, and ψ is the sample-space variable corresponding to ϕ.

The first term on the right-hand side, $\langle \Gamma\nabla^2\phi|\psi\rangle$, is the conditional diffusion of ϕ which represents the effects of molecular diffusion. The transport equation for the joint PDF of velocity, turbulence frequency, and composition is similar in form to Eq. (1), with the conditional diffusion term still being one of the unclosed terms. In both PDF methodologies, the reaction source term S is in closed form, while a mixing model is needed to account for the conditional diffusion.

A. Mixing models

Several mixing models have been developed to model the unclosed conditional diffusion term. Three of the most-widely used mixing models are: (i) the Interaction by Exchange with the Mean (IEM)[8,9] model, (ii) the Modified Curl (MC)[10,11] model, and (iii) the Euclidean Minimum Spanning Tree (EMST)[12] model. In the IEM model, particle compositions relax linearly toward the cell mean; in the MC model, particles within a cell are paired randomly and instantaneously mix; in the EMST model, a EMST is formed in composition space; particles mix with neighboring particles in the EMST so that the mixing remains local in composition space. The constant mechanical-to-scalar time scale ratio C_ϕ determines the mixing rate in all of these mixing models. The significance of C_ϕ here is that in the simple case of a statistically homogeneous conserved passive scalar, all mixing models yield the same rate of decay of the scalar variance. The development of novel mixing models is an area of active research, and several promising new models are being developed as well.[13–15]

The effects of mixing models have been studied in PDF calculations of a wide variety of reacting flows, including non-premixed lifted flames,[6,16] piloted non-premixed flames,[7] bluff-body non-premixed flames,[17] opposed-flow premixed flames,[18] piloted premixed jet flames,[19,20] and even high-pressure, premixed, homogeneous charge compression ignition engines.[21] Given the highly coupled nature of molecular diffusion and chemical reaction, these studies generally show significant sensitivity of the calculated flows to the choice of mixing model and value of C_ϕ. Typically, in parametric studies of mixing models such as these, calculations are performed using a variety of mixing models and values of C_ϕ, and the mean and RMS scalar fields are compared to experimental data.

B. Multiple scalar mixing

While studying the mixing processes and the effects of mixing models in the context of reacting flows is both interesting and practical, studying more fundamental mixing problems in non-reacting flows is also necessary. As experimental methods continue to improve, more experimental data on fundamental mixing problems has been available to test computational models. Testing in fundamental mixing problems is important because it provides a framework in which the mixing processes can be well understood, and where the computational models can be tested against real data. The most fundamental type of mixing study involves the mixing of two streams. The mixing state in this type of flow can be described by a single scalar, so this type of configuration is also referred to as the mixing of a single scalar, whereas flows with three or more streams are referred to as the mixing of multiple scalars. Much experimental research has been performed in two-stream mixing (the mixing of a single passive scalar)[22–28] including characterization of the mean and RMS statistics, as well as the PDF of the single scalar. Direct numerical simulation (DNS) has also been employed to study two-stream mixing[29–34] and in these studies, more complete information about the flow is extracted, in some cases including the conditional diffusion term.

In reacting flows, the mixing processes involve multiple scalars. The flows in most practical combustion devices require a combination of a fuel stream, an oxidizer stream, a pilot stream, and at least one coflowing stream. So, the fundamental studies of two-stream, single-scalar mixing have been expanded upon. The mixing of three streams has been studied experimentally[35,36] and computationally using DNS[37–39] and PDF methods.[40] In Ref. 40, the DNS of the temporally evolving three-stream mixing layer[39] is studied using the joint velocity-composition PDF for several different mixing models. It is found here that the IEM mixing model conditioned on velocity (IECM)[41–43] and a mixing model based on parameterized scalar profiles (PSP)[13,15] both outperform the standard IEM mixing model. The joint PDFs of the two scalars and the conditional diffusion from these two models show substantially better agreement with the DNS data.

Recent advances in experimental techniques, such as high-resolution planar laser-induced fluorescence (PLIF) imaging, have enabled experiments in which statistics more insightful than mean and RMS measurements can be extracted. The experiment in Ref. 36 considers the mixing of two scalars in a turbulent coaxial jet; this experiment utilizes PLIF and Rayleigh scattering to obtain high-resolution images of instantaneous mixture fractions, enabling the conditional diffusion and conditional scalar dissipation rate to be computed experimentally. The fundamental problem is essentially the same as the temporally evolving three-stream mixing layer studied with DNS in Ref. 39 and the joint-PDF method in Ref. 40, except that flow is[36] is spatially evolving, not temporally evolving, and is in fact a real, physical problem, as opposed to a purely numerical problem.

In multiple scalar mixing problems, the arrangement of the scalars plays an important role in determining the mixing process. The turbulent coaxial jet in Ref. 36 is useful because the configuration mimics that in combustion devices and many rudimentary turbulent jet flames: Two streams (the jet and the coflow) are initially separated by a third stream (the annulus), so that the mixing between two of the three streams (the jet and the coflow) can only occur through interaction with the other stream (the annulus). The turbulent coaxial jet of Ref. 36 is the basis for this study, and the detailed experimental configuration and procedure are described are Sec. II.

C. Objectives

The goals of this work are (i) to perform PDF calculations of the coaxial jet studied experimentally in Ref. 36, (ii) to evaluate the efficacy of three standard mixing models (IEM, MC, and EMST) by calculating the conditional diffusion in the PDF calculations and comparing it to the experimentally observed conditional diffusion, (iii) to assess the two-dimensional measurements of conditional diffusion and scalar dissipation rate through Large Eddy Simulation (LES) of varying resolution, and lastly, (iv) to examine the behavior of the mixing models used in LES-PDF calculations by evaluating the sensitivity to model parameters and examining a new model for the turbulent diffusivity redistribution.

While Reynolds-Averaged Navier Stokes (RANS)-based PDF methods have been studied carefully in the past, there remain many open questions about the performance of mixing models in LES-PDF calculations. These questions include the effect of the small scales on the mixing process, the effect of molecular diffusion on mixing, the optimal value of the scalar-to-mechanical timescale ratio, and the proper modeling of the turbulent mixing process. Objective (iv) listed above is directed to address some of these issues by carefully examining calculations of this flow and comparing the results to the experimental data. The approach used in this study has advantages over the other parametric studies of mixing models in reacting flows[6,7,16–21] because the conditional diffusion term can be explicitly compared to the experimental data; additionally, the flow can be studied apart from the complexities associated with chemical reaction. And although the configuration is similar to PDF comparison to the DNS data given in Ref. 40, here the configuration is a coaxial jet (as opposed to a mixing layer); furthermore, here the results can be compared to experimental data, which is important in ensuring that all the real physical processes are accounted for correctly in the model.

The remainder of this paper is outlined as follows: In Sec. II, the configuration of the flow and the experimental procedures used in Ref. 36 are described. Next, in Sec. III, the RANS-PDF framework is presented, the calculations are described, and the results are shown for different mixing models. In Secs. IV and V, the LES and LES-PDF calculations are presented. Finally, a comparison

TABLE I. Properties of inflowing streams in the three-stream mixing jet. The density and kinematic viscosity are computed using Chemkin based on the mass fractions, *Y*, indicated here.

Stream name	Jet	Annulus	Coflow
Inner diameter (mm)	. . .	6.35	9.50
Outer diameter (mm)	5.54	8.38	150
Bulk velocity (m/s)	34.5	32.5	0.4
Density (kg/m^3)	1.26	1.14	1.17
Viscosity (m^2/s × 10^{-6})	13.4	8.3	15.9
$Y_{C_3H_6O}$	0.132	0	0
$Y_{C_2H_4}$	0	1	0
Y_{N_2}	0.666	0	0.767
Y_{O_2}	0.202	0	0.233

between all three calculation methodologies is discussed in Sec. VI, and conclusions are drawn in Sec. VII.

II. FLOW CONFIGURATION

The flow studied in this work is based on the experiment conducted in Ref. 36, and consists of three concentric streams: a jet, an annulus, and a coflow. The central jet consists of acetone-doped air (7% acetone by volume) at a high velocity (34.5 m/s); surrounding the central jet is an annular flow of pure ethylene, also at a high velocity (32.5 m/s); surrounding the annulus is a coflow of air at a low velocity (0.4 m/s). The outer diameter of the coflow is sufficiently large so that the jet and annulus streams do not interact with the ambient air. Detailed properties of the configuration are shown in Table I. The diameter of the jet, *D*, is 5.54 mm and is used as a reference length scale throughout this study. The maximum density ratio is 1.11, and the Reynolds number (based on the jet composition, diameter, and bulk velocity) is 14 300.

In the experiment, simultaneous measurements of the acetone and ethylene mass fractions are made using two-dimensional planar imaging. The mass fraction of the acetone is obtained using PLIF, while the mass fraction of ethylene is obtained from Rayleigh scattering. The measurements are made with a spatial resolution of 55 μm. Time-averaged means and RMS statistics of the acetone and ethylene mass fractions are computed from the high-resolution images.

We denote by ξ_1, ξ_2, and ξ_3 the mixture fraction based on the jet, the annulus, and the coflow, respectively. Only two of these are independent (since $\xi_1 + \xi_2 + \xi_3 = 1$), and henceforth we consider ξ_1 and ξ_2. The jet mixture fraction, ξ_1, represents the fraction of mass originating from the central jet. It is approximated here as $\xi_1 = Y_{C_3H_6O}/Y^1_{C_3H_6O}$, where $Y_{C_3H_6O}$ is the mass fraction of acetone, and $Y^1_{C_3H_6O}$ is the mass fraction of acetone in the jet. In reality, the air and acetone have different diffusivities. The two substances will diffuse at different rates, and therefore the total mass originating from that stream may not be directly proportional to the amount of acetone present. However, the difference in molecular diffusivities is small (see Figure 11), and furthermore in this flow the turbulent diffusion dominates over the molecular diffusion. So this approximation of the mixture fraction is reasonable. The annulus mixture fraction, ξ_2, represents the fraction of mass originating from the annulus. Because the annulus contains only pure ethylene, ξ_2 is defined simply as $\xi_2 = Y_{C_2H_4}$, where $Y_{C_2H_4}$ is the mass fraction of ethylene.

The scalar dissipation rate, $\chi = 2\Gamma(\partial\xi/\partial x_i)(\partial\xi/\partial x_i)$, and the scalar diffusion term, $D = \Gamma\nabla^2\xi$, are both computed for ξ_1 and ξ_2 in the two components of the sampled images using a tenth-order central difference scheme. The term Γ is the molecular diffusivity of the scalar. In the evaluation of χ and *D* in the experiment, a constant value is used for the diffusivity of each scalar: $\Gamma_1 = 10.39 \times 10^{-6}$ m^2/s and $\Gamma_2 = 14.69 \times 10^{-6}$ m^2/s. The conditional scalar dissipation rate, $\langle\chi|\xi = \hat{\xi}\rangle$, where the angle brackets denote an ensemble average and $\hat{\xi}$ is a sample-space variable, and the conditional diffusion, $\langle D|\xi = \hat{\xi}\rangle$, are recorded from between 3000 and 5400 sampled images.

An uncertainty analysis performed in Ref. 36 shows the RMS fluctuations in the combined noise and uncertainty are around 2% for the mean and RMS scalar statistics. The scalar dissipation rate is corrected for measurement noise, and by examining finite-difference schemes of varying order, it is estimated that the scalar dissipation rate is at least 98% resolved in the experimental measurements.

III. RANS-PDF CALCULATIONS

A. RANS-based joint PDF methodology

This flow is first investigated computationally using the joint velocity-turbulence frequency-composition PDF method with RANS-level turbulence closure.[1,44] Throughout this paper, this method is referred to simply as the RANS-PDF method. In the implementation of this method,[47] a finite-volume solver evaluates the mean equations of mass, momentum, energy, and state while a Lagrangian Monte Carlo particle solver advances particles in velocity, turbulence frequency, and composition to solve for the joint PDF of velocity, turbulence frequency, and composition. More complete description of the methodology is provided in Ref. 47.

In the particle solver, the particle velocity evolves via the simplified Langevin model (SLM),[45] while the particle turbulence frequency evolves by a stochastic frequency model.[46] The stochastic frequency model relies on a number of parameters, and the standard values are used for each parameter as in many previous studies;[6,7,17,20] for the constant $C_{\omega 1}$, which essentially controls the spreading rate of the jet, a value of $C_{\omega 1} = 0.65$ is used based on a parametric study made to achieve the correct jet spreading rate. This value is well within the range of values (from $C_{\omega 1} = 0.56$[17] to $C_{\omega 1} = 0.70$[20]) used in similar studies, and is identical to the value used in Refs. 6 and 7. A list of the model constants used here, and described in more detail in Ref. 47, is shown in Table II.

The composition will generally evolve due to both molecular diffusion and chemical reaction. The main advantage of the PDF method is that the chemical reaction can be treated without modeling; in this case, the flow is inert, so there is no chemical reaction term. The density of a particle, ρ^* is computed through the relation

$$\rho^* = 1/\left(\xi_1^* (1/\rho_1) + \xi_2^* (1/\rho_2) + \xi_3^* (1/\rho_3)\right), \tag{2}$$

where ξ_1^*, ξ_2^*, and ξ_3^* are mixture fractions for the particle, and ρ_1, ρ_2, and ρ_3 are the densities of the three streams from Table I. Equation (2) essentially states that the specific volume of the mixture is equal to the mass-fraction-weighted specific volume of each component of that mixture, as the fluid is considered to be an ideal gas. The effect of molecular diffusion on the particle composition is treated by a mixing model. Here, the IEM, MC, and EMST mixing models are examined, with the IEM being used for the base case.

In the implementation of this method, finite-volume and particle solvers are coupled. The finite-volume solver provides the mean velocity, density, and pressure to the particle solver, while the particle solver provides the turbulent fluxes and the reaction source term (which in this case is zero, since the flow is non-reacting). When a statistically stationary state is reached in the calculations, the statistics are time-averaged until sufficient temporal convergence of the statistics is reached.

TABLE II. Model constants for base-case RANS-PDF calculations.

Constant	Value	Usage
C_0	2.1	SLM
C_Ω	0.6893	Definition of the mean frequency Ω
$C_{\omega 1}$	0.65	Turbulence frequency model
$C_{\omega 2}$	0.90	Turbulence frequency model
C_3	1.0	Turbulence frequency model
C_4	0.25	Turbulence frequency model
C_ϕ	1.5	EMST mixing model

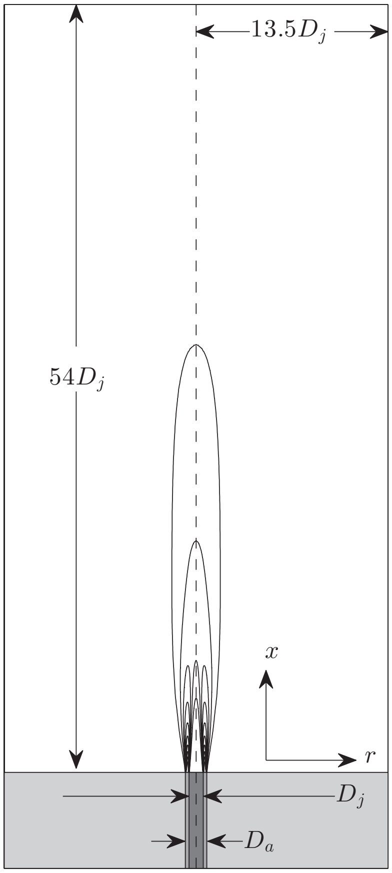

FIG. 1. Computational domain for RANS-PDF calculations. The contour represents the mean mixture fraction of the annulus stream.

B. Computational configuration

To model this flow, a rectangular computational domain extending 54*D* in the axial (x) direction and 13.5*D* in the radial (r) direction is used. Figure 1 shows a sketch of the computational domain. This size is chosen based on a parametric study of domain sizes, where the statistics of interest (mean and RMS mixture fractions at x/D of 30, near the farthest-downstream measurement in the experiment) are not significantly affected by the outlet boundary condition and the lateral boundary condition.

The lateral boundary condition ($r/D = 13.5$) is treated as a perfect-slip wall, and symmetry conditions are applied at the axis ($r/D = 0$). For the outlet boundary condition ($x/D = 54$), the mean pressure is specified to be uniform, and the density and velocities are extrapolated from the interior. At the inflow boundary ($x/D = 0$), the mean velocities, Reynolds stresses, and turbulence frequency are specified from a separate calculation using a 5-equation Reynolds-stress equation turbulence model. These calculations extend upstream beyond the inflow plane, and the flow of the pipe and the annulus are fully developed flows. In these calculations, plug flow profiles are applied for the three streams 60 jet diameters upstream of the jet exit plane. The standard Reynolds-stress model[48,49] in the commercial code Fluent is used with the constants $C_{1\epsilon} = 1.60$, $C_{2\epsilon} = 1.92$, $C_\mu = 0.90$, $C_1 = 1.80$, $C_2 = 0.60$, $\sigma_k = 1.0$, and $\sigma_\epsilon = 1.3$. The calculations are tested for numerical accuracy through temporal convergence and grid convergence studies. The mean velocities, Reynolds-stresses, and turbulent frequency along the jet exit plane are extracted for use as an inflow boundary condition for the PDF calculations.

Figure 2 shows the mean axial velocity and three of the Reynolds-stresses at the inflow plane. The composition at the inflow boundary is specified as in Table I. The joint PDF of the velocity is

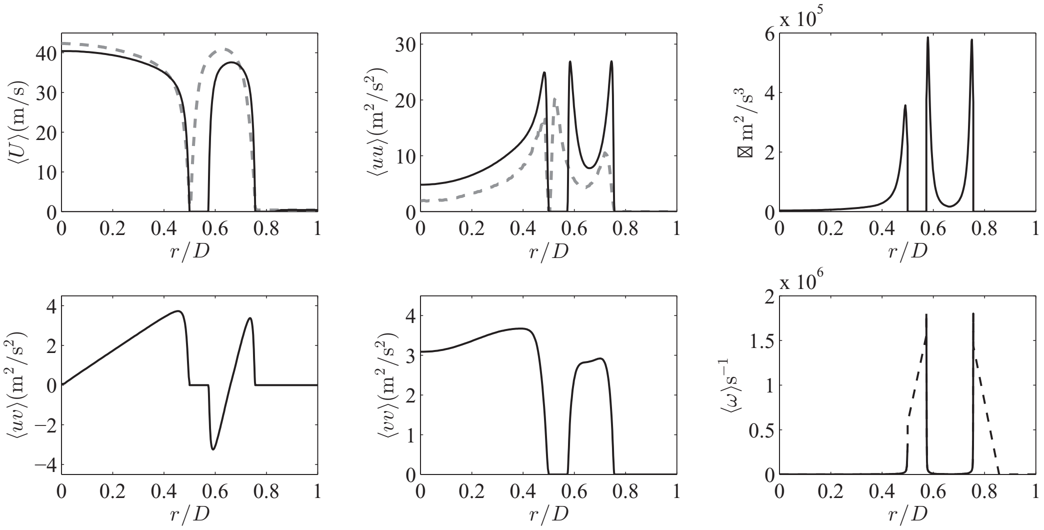

FIG. 2. Boundary conditions for RANS-PDF calculations in solid lines: the mean axial velocity, $\langle U\rangle$, (top-left) and the Reynolds stresses $\langle uu\rangle$ (top-middle), $\langle uv\rangle$ (bottom-left), and $\langle vv\rangle$ (bottom-middle), the dissipation rate (top-right), and the mean turbulence frequency (bottom-right). The gray dashed lines represent quantities from the LES calculations (which do not include the jet wall thickness) to be discussed later in this work.

taken to be joint-normal at the inflow boundary condition, and the PDF of the turbulence frequency is a gamma function of the specified mean and variance, statistically independent from the velocity.

At 64 locations throughout the flow domain, the joint PDF of ξ_1 and ξ_2 and the conditional diffusion of ξ_1 and ξ_2 are calculated. The sampled locations include 32 points along the jet centerline ($r/D = 0$), and 16 points each along radial profiles at $x/D = 3.29$ and $x/D = 6.99$. Each location at which measurements are made in Ref. 36 is accounted for. At every time step during the statistically stationary period during which statistics are collected, particles within a rectangle extending 275 μm (about 0.05D) in the radial direction and 495 μm (about 0.09D) in the axial direction centered about a sampling location are sampled at that location. The spatial extent of this sampling range is equivalent to the resolution used in the experiments for computing the conditional statistics. Each sampled particle is binned into 1 of 400 equally spaced bins, for each component of the two-dimensional mixture fraction space ranging from 0 to 1. The conditional diffusion for ξ_1 and ξ_2 is calculated as the change in ξ_1 and ξ_2 over the mixing sub-step, divided by the time step.

C. Numerical accuracy and comparison with experimental data

1. Grid convergence

The numerical accuracy of the calculations is affected by (i) the grid size, (ii) the number of particles per cell, (iii) the duration over which time-averaging is performed, and (iv) the time step. The first three of these error sources are systematically tested, and a numerical error is computed for statistics of interest. The fourth error source, the time step, is tested indirectly as the grid is refined. In these tests, an error is evaluated for the statistics $\langle\widetilde{\xi_1}\rangle$, $\langle\widetilde{\xi_2}\rangle$, $\langle\widetilde{\xi_1''}\rangle$, and $\langle\widetilde{\xi_2''}\rangle$. In the notation used here, the angle brackets ⟨⟩ denote a time-averaged quantity, the tilde ˜ denotes a mass-weighted quantity, and the double-prime ″ denotes the RMS; so $\langle\widetilde{\xi_1}\rangle$ is the time-averaged mass-weighted mean of ξ_1 and $\langle\widetilde{\xi_1''}\rangle$ is the time-averaged mass-weighted RMS of ξ_1. The errors defined for each of these four quantities are denoted by ϵ_{M1}, ϵ_{M2}, ϵ_{R1}, and ϵ_{R2}, respectively. The error for each statistic is defined as the maximum value of the difference between that statistic and the value of that statistic in the most numerically accurate solution for the range $3.29 \leq x/D \leq 6.99$.

Tests are performed with 25, 50, 100, and 200 particles per cell, with grids ranging from 64 × 64 to 384 × 384, and for durations of time-averaging between 1000 and 20 000 iterations. In the tests, the IEM mixing model is used with a value of C_ϕ of 1.5, and other convergence studies

TABLE III. Grid sizes (number of cells in x and r, n_x, and n_r, and total number of cells in thousands, n_T) and errors from convergence tests of the RANS-PDF calculations.

Grid name	n_x	n_r	n_T	ϵ_{M1}	ϵ_{M2}	ϵ_{R1}	ϵ_{R2}
G-1	64	64	4.1	0.125	0.175	0.089	0.043
G-2	96	96	9.2	0.091	0.086	0.065	0.029
G-3	128	128	16.4	0.061	0.043	0.044	0.021
G-4	192	192	36.9	0.024	0.016	0.020	0.009
G-5	256	256	65.5	0.016	0.010	0.013	0.008
G-6	384	384	147.5	...	...	...	...

have verified the behavior with IEM is representative of those calculations using other mixing models. These tests show that the largest source of error is in the grid resolution. The grid sizes and corresponding numerical errors are shown in Table III. As the grid is refined, the errors for all statistics are successively reduced. For grid G-4, the numerical error in all statistics is around 2%, which is close to the experimental error. Based on these convergence tests, the parameters chosen for the base case calculations are 100 particles per cell, a grid size of 192 × 192, and a minimum of 10 000 iterations of time-averaging.

2. Comparison with experimental data

Figure 3 shows statistics of mean and RMS quantities on the jet centerline ($r/D = 0$) for four of the grids in Table III and the experimental data.[36] On the finest grids, $\langle\widetilde{\xi_1}\rangle$ and $\langle\widetilde{\xi_2}\rangle$ exhibit good agreement with the experimental data. The largest discrepancy between the experimental data and the numerically accurate calculations is about 6% at $x/D = 6.99$, where the initial spreading of the jet is slightly more rapid in the calculations than in the experiments. For the RMS statistics,

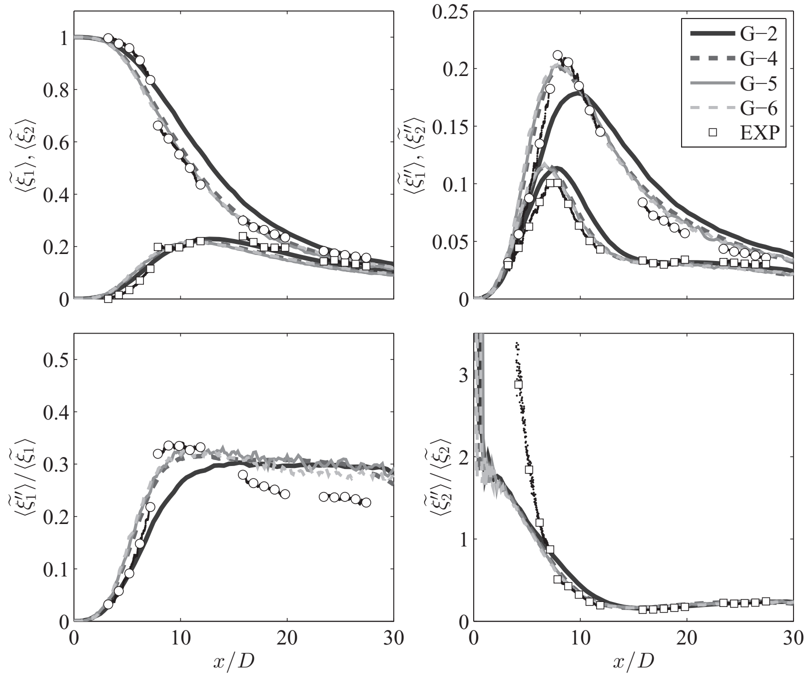

FIG. 3. Centerline profile of time-averaged mass-weighted mean mixture fractions (top left), RMS mixture fractions (top right), and fluctuation intensities (bottom) in the RANS-PDF grid convergence study. Solid dark line: G-2; dashed dark line: G-4; solid gray line: G-5; dashed light gray line: G-6; circles: experimental data for ξ_1;[36] squares: experimental data for ξ_2.[36]

the agreement on the centerline is also reasonable; here too, the largest disagreement occurs in the near-field of the jet, where the RMS is slightly overpredicted in the calculations.

Figure 3 also shows the fluctuation intensities, $\langle \widetilde{\xi_1''} \rangle$ / $\langle \widetilde{\xi_1} \rangle$ and $\langle \widetilde{\xi_2''} \rangle$ / $\langle \widetilde{\xi_2} \rangle$. In the PDF calculations, the peak fluctuation intensity of ξ_1 is captured well. However, the measurements indicate the fluctuation approaching an asymptotic value near 0.21 downstream (in the far field of the jet), in accord with the self-similar region in binary jet mixing.[26,35] Here, the PDF calculations over-estimate the fluctuation intensity, due to the values of both C_ϕ and $C_{\omega 1}$ used in the calculations. A slightly larger value of C_ϕ leads to decreased variance and hence decreased fluctuation intensity, while a slightly larger value of $C_{\omega 1}$ leads to a decreased spreading rate of the jet, an increased mean ξ_1 downstream, and consequentially a decreased fluctuation intensity. The fluctuation intensity of ξ_2, on the other hand, demonstrates good consistency with the experimentally observed values downstream, and does approach the value observed in the self-similar region of binary jet mixing, around 0.21. In the near-field, however, there is considerable variation among the calculations and the experimental data, due to the small values of $\langle \widetilde{\xi_2} \rangle$ and the sensitivity to the inflow boundary conditions. There is also more numerical error observed in the calculations of the fluctuation intensities here, mostly arising from the combination of insufficient time-averaging and low values of the mean farther downstream.

Figure 4 shows the radial profiles of $\langle \widetilde{\xi_1} \rangle$, $\langle \widetilde{\xi_2} \rangle$, $\langle \widetilde{\xi_1''} \rangle$, and $\langle \widetilde{\xi_2''} \rangle$ for the same PDF calculations and the experimental data. As noted from Figure 3, $\langle \widetilde{\xi_1} \rangle$ decays slightly faster in the PDF calculations than as measured experimentally. However, Figure 4 shows that this is limited to a small region near the jet centerline. The agreement in $\langle \widetilde{\xi_2} \rangle$ is also reasonable, although the peak value, which occurs around $r/D = 0.6$ is slightly under-predicted in the calculations due to the annulus spreading slightly faster in the calculations.

The RMS statistics, shown in Figure 4(b), indicate the peak RMS of both ξ_1 and ξ_2 being overpredicted at $x/D = 3.29$, but farther downstream at $x/D = 6.99$ the agreement in the peak RMS is good for both ξ_1 and ξ_2. The overprediction at $x/D = 3.29$ is a result of both the inlet boundary conditions, which are sensitive to the value of ω, the turbulence frequency, and the mixing model. The values of $\langle \widetilde{\xi_1''} \rangle$ from the calculations are in very good agreement with that from the experiments at $x/D = 6.99$. The values of $\langle \widetilde{\xi_2''} \rangle$ from the calculations are in reasonable agreement with the experimental data at $x/D = 6.99$ in the region of jet-annulus mixing ($0 \le r/D \le 1$), but not in the region of annulus-coflow mixing ($r/D > 1$). In the region of annulus-coflow mixing for all these

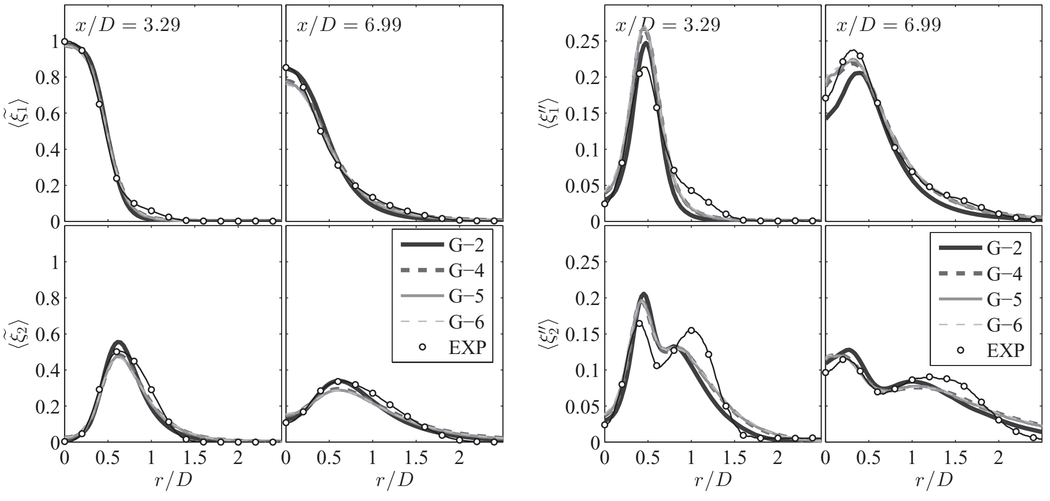

(a) (b)

FIG. 4. Radial profiles of time-averaged mass-weighted mean (a) and RMS (b) mixture fractions in the RANS-PDF grid convergence study. Solid dark line: G-2; dashed dark line: G-4; solid gray line: G-5; dashed light gray line: G-6; circles: experimental data.[36]

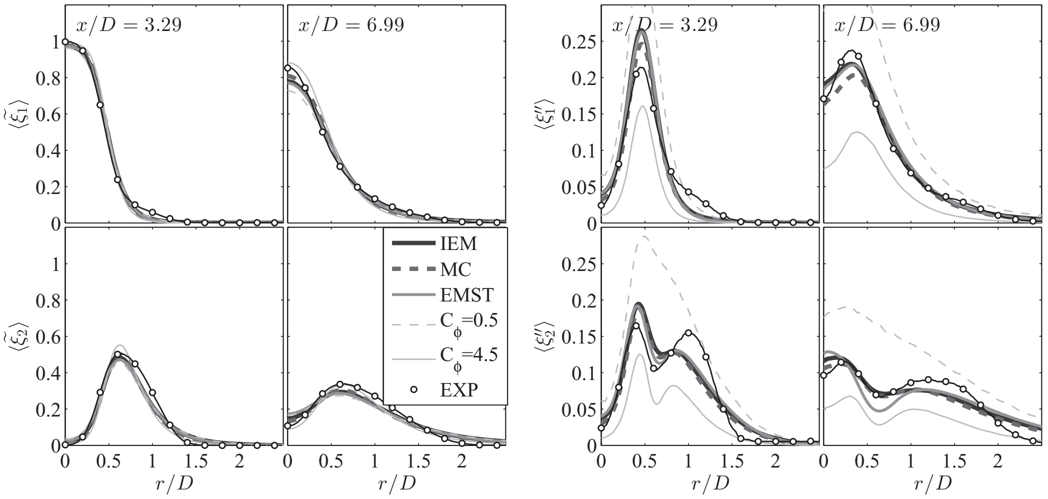

(a) (b)

FIG. 5. Radial profiles of time-averaged mass-weighted mean (a) and RMS (b) mixture fractions in the RANS-PDF mixing model study. Solid dark line: IEM, $C_\phi = 1.5$; dashed dark line: MC, $C_\phi = 1.5$; solid gray line: EMST, $C_\phi = 1.5$; dashed light gray line: IEM, $C_\phi = 0.5$; light gray solid line: IEM, $C_\phi = 4.5$; circles: experimental data.[36]

axial locations, the profile of $\langle\widetilde{\xi}_2''\rangle$ is much sharper in the experimental data; in the regions where $\langle\widetilde{\xi}_2''\rangle$ is large, the calculations yield a smaller value; in the regions where $\langle\widetilde{\xi}_2''\rangle$ is small, the calculations yield a larger value. This behavior is primarily due to the mixing models; in this region of the flow, molecular diffusion is important due to the very low velocity of the coflow; additionally, the mixing process is velocity dependent, so these mixing models, which do not consider the velocity, are likely to encounter difficulties where there is a large velocity gradient, as there is here.

D. Comparison of mixing models in the RANS-PDF calculations

Shown in Figure 5 are the results of calculations using the IEM mixing model and different values of C_ϕ, namely, C_ϕ of 0.5, 1.5, and 4.5. There is a small sensitivity of $\langle\widetilde{\xi}_1\rangle$ to the value of C_ϕ; larger values of C_ϕ result in a decreased jet spreading rate due to the decreased scalar flux. There is a much larger sensitivity to the RMS statistics, $\langle\widetilde{\xi}_1''\rangle$ and $\langle\widetilde{\xi}_2''\rangle$; larger values of C_ϕ yield a decreased RMS, which is expected since C_ϕ directly impacts the scalar variance. Figure 5 convincingly shows that in these calculations, a value of $C_\phi = 1.5$ yields both mean and RMS fields in the best agreement with the measurements. This value is in close agreement with the experimentally measured values, around 1.5 in inert round jets[28] and in the range 1.5–2.5 in shear flows.[23]

The other two mixing models (MC and EMST) are also used to make calculations of this flow, and the resulting centerline and radial profiles of the mean and RMS statistics are very similar to those using the IEM model. Figure 5 demonstrates the similarity of the radial profiles of the statistics $\langle\widetilde{\xi}_1\rangle$, $\langle\widetilde{\xi}_2\rangle$, $\langle\widetilde{\xi}_1''\rangle$, and $\langle\widetilde{\xi}_2''\rangle$ in the calculations with these three mixing models, all using a value of $C_\phi = 1.5$. The value of C_ϕ has a very similar effect among all three of these mixing models.

The correlation coefficient between the two mixture fractions, ρ_{12}, is defined as

$$\rho_{12} = \frac{\langle \xi_1 \xi_2 \rangle - \langle \xi_1 \rangle \langle \xi_2 \rangle}{\sqrt{\langle \xi_1^2 \rangle - \langle \xi_1 \rangle^2}\sqrt{\langle \xi_2^2 \rangle - \langle \xi_2 \rangle^2}} \tag{3}$$

and is shown in Figure 6 for these calculations and the experimental measurements. Around the centerline, ρ_{12} is approximately -1, since the mixture fraction of the coflow is very small. With a negligible coflow mixture fraction, the sum $\xi_1 + \xi_2$ is approximately unity, so ξ_1 and ξ_2 are nearly perfectly anti-correlated. All mixing models yield similar values of ρ_{12} near the centerline, and the agreement with the experimental data is good, considering the measurement noise evident

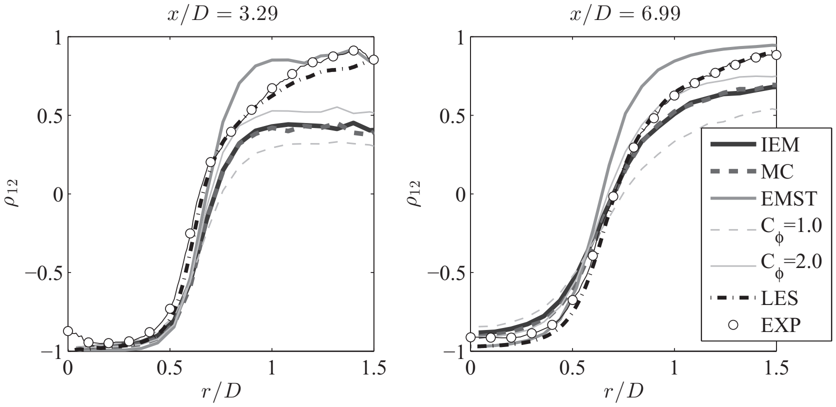

FIG. 6. Radial profiles of the correlation coefficient. Solid dark line: IEM, $C_\phi = 1.5$; dashed dark line: MC, $C_\phi = 1.5$; solid gray line: EMST, $C_\phi = 1.5$; dashed light gray line: IEM, $C_\phi = 1.0$; light gray solid line: IEM, $C_\phi = 2.0$; dashed-dotted line: LES on Grid-F; circles: experimental data.[36]

on the centerline. Going away from the centerline, the differences between the calculations are more pronounced. With EMST, the correlation coefficient increases at a faster rate (compared to the measurements and calculations with other mixing models) with increasing *r*/*D* beginning at about *r*/*D* = 0.75. The values of ρ_{12} with IEM and MC are very similar to one another, and at large values of *r*/*D*, both are much lower than that from EMST and the experimental measurements. At large values of *r*/*D*, both the mean and RMS of ξ_1 and ξ_2 are very low, so there is greater numerical uncertainty in these statistics. Figure 6 shows that as C_ϕ is increased, the radial profiles of the correlation coefficient become sharper. This observation is consistent with the fact that increasing C_ϕ decreases the scalar variance, and consequently reduces the spreading of the mixing layers. Figure 6 also shows the resolved ρ_{12} from LES calculations on the fine Grid-F. These calculations yield a correlation coefficient in very good agreement with the experimental data and are discussed more in detail in Sec. IV.

Despite the similarity in the mean and RMS statistics, there is considerable difference in the higher-order statistics for different mixing models. The joint PDFs and conditional diffusion of ξ_1 and ξ_2 yielded by each mixing model are markedly different. Figures 7 and 8 show the joint PDF and conditional diffusion from the experiments and calculations, with each figure from a different location: Figure 7 is from (*x*/*D* = 3.29, *r*/*D* = 0.536), and Figure 8 is from (*x*/*D* = 6.99, *r*/*D* = 0.635). These particular locations are chosen such that there is significant mixing of all three streams at those locations.

Compared to the experimental data, the IEM model yields a joint PDF which is more compact in composition space. At *x*/*D* = 6.99, the joint PDF from the calculations using IEM indicates a bimodal PDF, instead of the unimodal PDF as observed experimentally. This indicates the IEM producing a flapping behavior between the jet and coflow at this location; so even though the mean and RMS statistics are calculated reasonably accurately with the IEM model, the higher-order statistics are not. The shapes of the PDFs from the calculations with IEM are similar in form to what is observed in the joint PDF calculations using the IEM mixing model in the three-stream mixing layer studied in Ref. 40; in both calculations, the IEM model yields less spreading of the joint PDF in composition space. The conditional diffusion from the IEM model indicates values linearly proportional to the distance from the mean. This is consistent with the model formulation and helps to validate the calculation of the conditional diffusion in the PDF calculations. Although the conditional diffusion is quite different in form to the measured conditional diffusion (as it is expected for the IEM model), the magnitude of the conditional diffusion is of the same order of magnitude in both the calculations and the experiments.

The MC model yields a joint PDF which is qualitatively the most similar to the joint PDF observed experimentally at *x*/*D* = 6.99 (Figure 8). The main difference between the calculations with the MC model and the experimental data is that MC model yields a joint PDF that is distributed

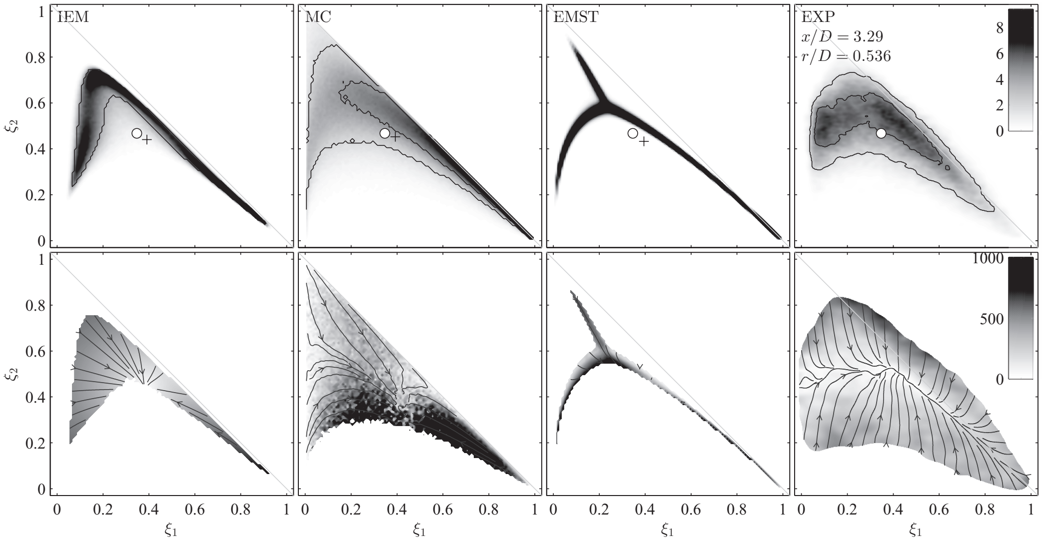

FIG. 7. Contour plots of the joint PDF of mixture fractions (top) and the magnitude of conditional diffusion (bottom) at (*x*/*D*, *r*/*D*) = (3.29, 0.536) from the experimental data[36] (right) and RANS-PDF calculations using different mixing models, from left to right: IEM, MC, and EMST. The circle is the experimental mean, and the plus sign is the mean from the PDF calculation. In the top plots, the two solid lines are isocontours which enclose regions with probability 0.5 and 0.9. In the lower plots, the lines with arrows are streamlines, everywhere parallel to the conditional diffusion vector.

more broadly over the composition space. Because the MC model involves a jump process in composition space during the mixing step, the values for the conditional diffusion calculated from the MC model can be highly dependent on the time-step. For this reason, there is a large variation in the computed values of the conditional diffusion.

The EMST mixing model yields the most interesting joint PDFs of all the mixing models studied here. With EMST, the joint PDFs are very compact, much more so than those from the IEM model or

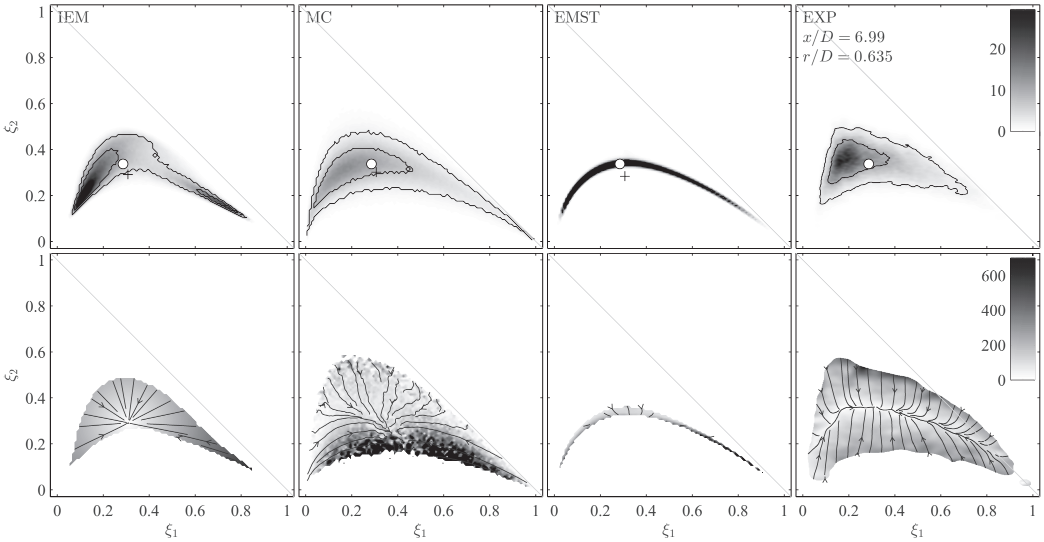

FIG. 8. Contour plots of the joint PDF of mixture fractions (top) and the magnitude of conditional diffusion (bottom) at (*x*/*D*, *r*/*D*) = (6.99, 0.635) from the experimental data[36] (right) and RANS-PDF calculations using different mixing models, from left to right: IEM, MC, and EMST. The circle is the experimental mean, and the plus sign is the mean from the PDF calculation. In the top plots, the two solid lines are isocontours which enclose regions with probability 0.5 and 0.9. In the lower plots, the lines with arrows are streamlines, everywhere parallel to the conditional diffusion vector.

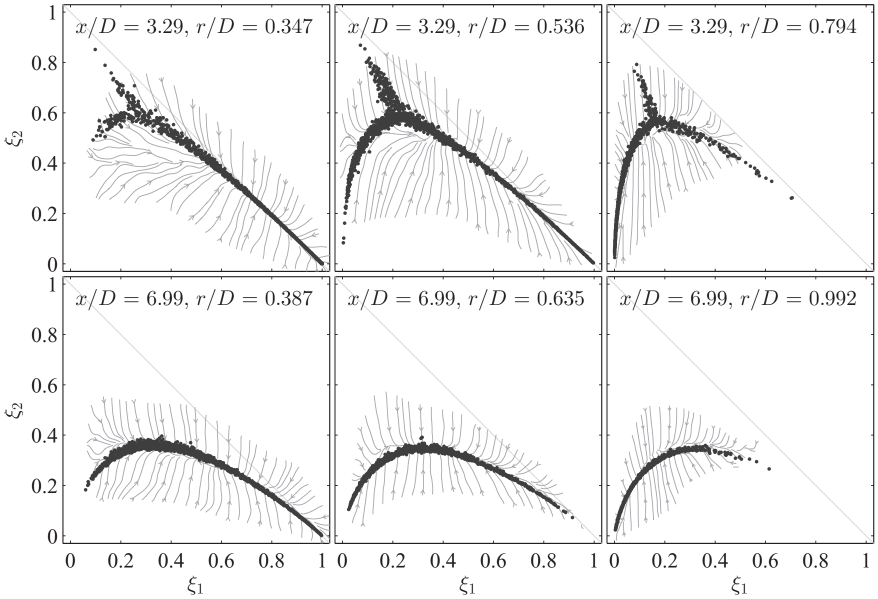

FIG. 9. Particle scatter plots in mixture fraction space from the RANS-PDF calculations using the EMST mixing model overlaid onto the conditional diffusion streamlines from the experimental data.

any of the mixing models studied in Ref. 40. The behavior observed is similar to that observed in the initial EMST development studies[12] and the joint PDF study in Ref. 14. More interesting, however, is the location in composition space at which the dense PDFs occur. The PDFs are concentrated in the region of the slow manifold identified experimentally. In Ref. 36 it is observed that for each scalar joint PDF, the mixture fractions are initially drawn in quickly toward a manifold of lower dimension in mixture fraction space. Here, the term fast-manifold is used to refer to the initial trajectories in mixture fraction space, whereas the term slow-manifold is used in reference to the single low-dimensional manifold to which all the fast manifolds are drawn.

Figure 9 demonstrates this through a scatter plot of particles from the calculations using EMST, onto which is overlaid the streamlines of conditional diffusion from the experiment. At all measured locations, the compositions yielded by the calculations using EMST lie almost directly on the slow manifold. This behavior suggests that the slow manifold exists at least in part due to mixing being local in composition space. Previous calculations of reacting flows in which the EMST mixing model yields more accurate calculations than the other mixing models[6,7] are partially attributed to this behavior of the EMST mixing model, along with the sensitivity of the chemistry to the location in mixture fraction space. The PDFs and conditional diffusion also show a complete lack of the fast manifold observed in the experiments. This suggests that other physical processes not accounted for in the EMST model, for example, differential diffusion, molecular transport, and velocity-conditioned mixing, are possibly responsible for the fast manifolds.

One of the drawbacks of the EMST mixing model is that it does not satisfy the condition of linearity;[12] in the EMST mixing model, the evolution equations for the particle properties of scalars are changed when the scalars are linearly transformed. The calculations of this coaxial jet are found to be sensitive to how the composition is described when the EMST model is used. Typically, in these types of RANS-PDF calculations, the composition is described by the specific mole fractions (the mass fraction divided by the molecular weight) and the sensible enthalpy. However, this formulation results in scalar fields vastly different than what is observed with the other mixing models (IEM and MC). This occurs because, in the specific mole composition space, the jet and coflow compositions are much closer to one another than to the annulus composition (as measured by the Euclidean norm). This biases the mixing between the jet and the coflow when the EMSTs are formed. To remedy this problem, the composition which undergoes mixing is defined to be the three mixture fractions. Figure 10 demonstrates why the latter formulation is more appropriate: when a EMST is formed

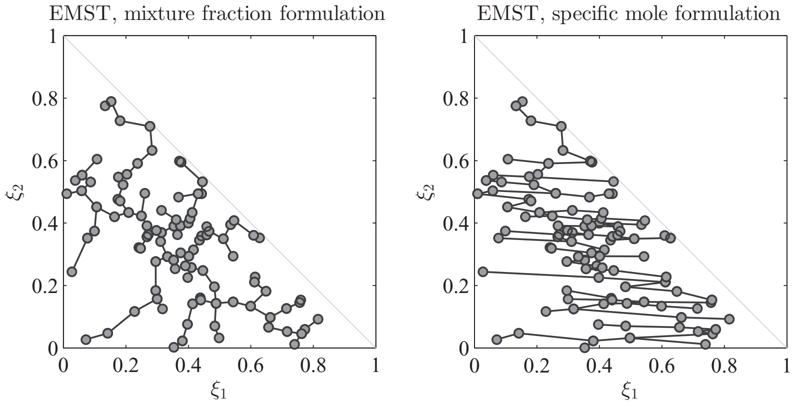

FIG. 10. Example of EMSTs formed in mixture fraction space using the two different EMST formulations: On the left, the mixed composition variables are the three mixture fractions; On the right, the mixed variables are the specific moles of the four chemical species, C_3H_6O (acetone), C_2H_4 (ethylene), N_2, and O_2.

using the original formulation (species specific moles), the EMSTs bias jet-coflow mixing; with the formulation used here (three mixture fractions), there is no bias between any pair of the three streams because the composition of each stream is equidistant in composition space from each other stream. This deficiency of the EMST mixing model must be called into consideration for multiple-stream mixing problems, particularly when the composition of one stream is far in composition space from that of the other streams.

The RANS-PDF studies of these three mixing models demonstrate the strengths and weaknesses of each model in this flow. All three models yield mean and RMS statistics in good agreement with the experimental data, but only the EMST mixing model yields compositions on the slow manifold identified in the experimental study. There is room for improvement in the predictions of the joint PDFs; based on the comparisons between the results here and those in Ref. 40, the newly developed IECM and PSP mixing models appear to be good candidates for improved performance.

IV. LES CALCULATIONS

In addition to RANS-based approaches, LES can also be used in conjunction with PDF methods. In LES, the large scales of the turbulence are resolved, and the small scales must be modeled. Since the large scales contain most of the kinetic energy of the flow, most of the large-scale features of the flow can be resolved. The LES-PDF methodology has many benefits over RANS-PDF in that it can more robustly treat flows with complex geometry, recirculating or swirling flows, and unsteady flows. Additionally, an advantage of the LES-PDF methodology over pure LES is that chemical reaction can be treated without modeling; this is especially important for LES, where most chemical reaction takes place on the unresolved scales.

The primary purpose of this study is to examine the effects of modeling the molecular diffusion in LES-PDF; the LES calculations are used to set up the LES-PDF calculations, to gauge the significance of the grid resolution on the results, and to provide an intermediate comparison between the LES-PDF calculations and the experimental measurements. This intermediate comparison is particularly valuable here, where challenging experimental measurements (including the conditional diffusion and scalar dissipation rate) are made and must be evaluated carefully with respect to their own resolution.

A. LES methodology

In the LES performed here, a system of equations is solved for the resolved density-weighted velocity, $\widetilde{\mathbf{U}}$, and the resolved density, $\bar{\rho}$.[50] These are the resolved equations for conservation of mass,

$$\frac{\partial \bar{\rho}}{\partial t} + \frac{\partial \bar{\rho}\widetilde{U}_j}{\partial x_j} = 0, \tag{4}$$

and conservation of momentum,

$$\frac{\partial \bar{\rho}\widetilde{U}_i}{\partial t} + \frac{\partial \bar{\rho}\widetilde{U}_i\widetilde{U}_j}{\partial x_j} = -\frac{\partial \bar{P}}{\partial x_i} + 2\frac{\partial}{\partial x_j}\left(\bar{\rho}\left(\widetilde{\nu} + \nu_T\right)\left(\widetilde{S}_{ij} - \frac{1}{3}\widetilde{S}_{kk}\delta_{ij}\right)\right), \tag{5}$$

where $\bar{P}$ is the volume-weighted resolved pressure, $\widetilde{\nu}$ is the resolved molecular viscosity, ν_T is the turbulent viscosity, and $\widetilde{S}_{ij}$ is the resolved strain rate. In this flow, there are two independent conserved scalar variables (the jet and the annulus mixture fractions, ξ_1 and ξ_2, respectively), so an additional transport equation,

$$\frac{\partial \bar{\rho}\widetilde{\xi}}{\partial t} + \frac{\partial \bar{\rho}\widetilde{U}_j\widetilde{\xi}}{\partial x_j} = \frac{\partial}{\partial x_j}\left(\bar{\rho}\left(\widetilde{\Gamma} + \Gamma_T\right)\frac{\partial \widetilde{\xi}}{\partial x_j}\right), \tag{6}$$

is solved for each density-weighted resolved mixture fraction, $\widetilde{\xi}$. In Eq. (6), $\widetilde{\Gamma}$ is the resolved molecular diffusivity of the mixture fraction, and Γ_T is the turbulent diffusivity. An additional transport equation for the variance of each mixture fraction, $V_\xi = \widetilde{\xi^2} - \left(\widetilde{\xi}\right)^2$, in the form of

$$\frac{\partial \bar{\rho} V_\xi}{\partial t} + \frac{\partial \bar{\rho}\widetilde{U}_j V_\xi}{\partial x_j} = \frac{\partial}{\partial x_j}\left(\bar{\rho}\left(\widetilde{\Gamma} + \Gamma_T\right)\frac{\partial V_\xi}{\partial x_j}\right) - \bar{\rho}\widetilde{\chi} + 2\bar{\rho}\left(\widetilde{\Gamma} + \Gamma_T\right)\frac{\partial \widetilde{\xi}}{\partial x_j}\frac{\partial \widetilde{\xi}}{\partial x_j}, \tag{7}$$

is solved for each scalar as well. In Eq. (7), $\widetilde{\chi}$ is the scalar dissipation rate, which is modeled here in a similar way as in Refs. 52, 53, and 58,

$$\widetilde{\chi} = \widetilde{\chi}_R + C\left(\frac{\Gamma_T + C_D\widetilde{\Gamma}}{\Delta^2}\right)V_\xi, \tag{8}$$

where Δ is the characteristic turbulence resolution scale, and $\widetilde{\chi}_R$ is the resolved scalar dissipation rate, which is given by

$$\widetilde{\chi}_R = 2\widetilde{\Gamma}\frac{\partial \widetilde{\xi}}{\partial x_j}\frac{\partial \widetilde{\xi}}{\partial x_j}. \tag{9}$$

The standard value of 2.0 is used for the constant C as in Ref. 53, and a value of 2.0 is used for the constant C_D. The resolved density is computed from Eq. (2) based on the resolved mixture fractions. The turbulent viscosity is computed according to the dynamic procedure in Refs. 54 and 55; although the algebraic model in Ref. 56 is also assessed in this flow. The turbulent diffusivity is computed from the turbulent viscosity using a turbulent Schmidt number, Sc_T, of 0.4 as in other similar studies.[53,57,59] The molecular viscosity and molecular diffusivities are evaluated from second-order polynomial curve-fits to data from Chemkin's Tranlib, in the form of

$$\nu = \nu_0\left(a_1 + a_2\xi_1 + a_3\xi_2 + a_4\xi_1^2 + a_5\xi_2^2 + a_6\xi_1\xi_2\right) \tag{10}$$

for the molecular viscosity, and

$$\Gamma = \Gamma_0\left(a_1 + a_2\xi_1 + a_3\xi_2 + a_4\xi_1^2 + a_5\xi_2^2 + a_6\xi_1\xi_2\right) \tag{11}$$

for each molecular diffusivity. The fitting error is less than 2%. The coefficients used in the curve-fits are shown in Table IV.

In the experimental work, constant values are used for the diffusivity of acetone, Γ_1^e, and ethylene, Γ_2^e to evaluate the conditional diffusion and scalar dissipation rates. These values, which are obtained from experimental correlations, are $\Gamma_1^e = 10.4\times 10^{-6}\ \mathrm{m^2/s}$ and $\Gamma_2^e = 14.7\times 10^{-6}\ \mathrm{m^2/s}$. For acetone, Γ_1^e is in reasonable agreement with the value computed here numerically at the composition of the

TABLE IV. Coefficients to curve-fits for molecular viscosity and molecular diffusivities of jet and annulus mixture fractions.

		a_1	a_2	a_3	a_4	a_5	a_6
ν	$\nu_0 = 15.9 \times 10^{-6}\ \mathrm{m^2/s}$	1.00	−0.165	−0.618	0.009	0.179	0.087
Γ_1	$\Gamma_{10} = 9.79 \times 10^{-6}\ \mathrm{m^2/s}$	1.00	−0.067	−0.363	−0.001	0.099	−0.015
Γ_2	$\Gamma_{20} = 16.1 \times 10^{-6}\ \mathrm{m^2/s}$	1.00	−0.079	0.041	0.002	−0.019	−0.037

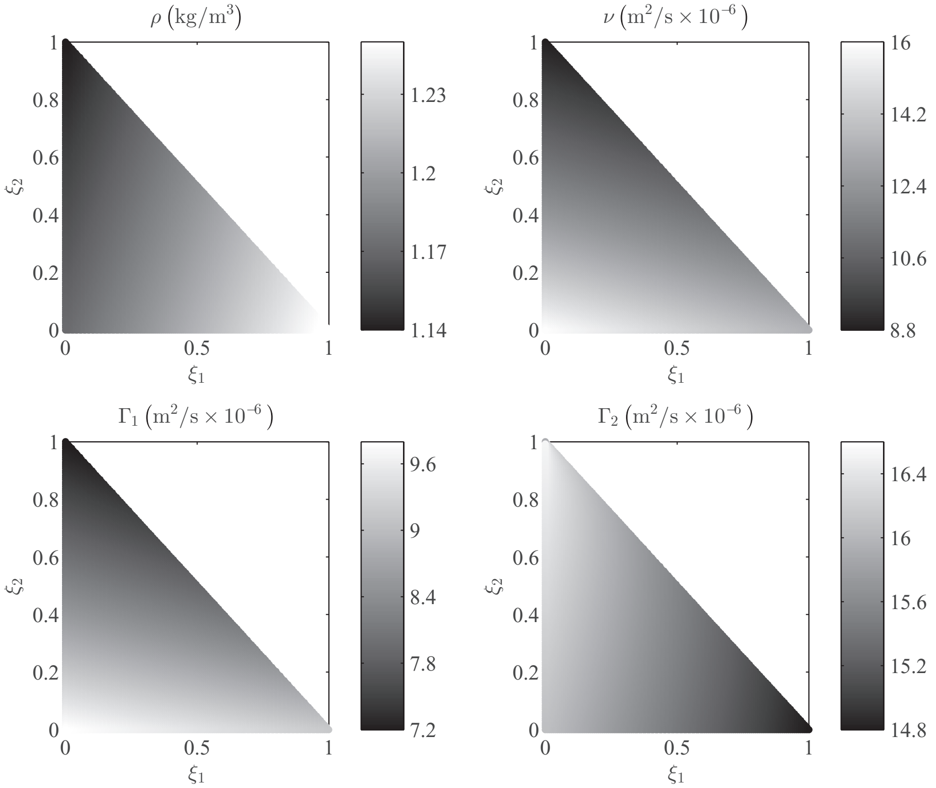

FIG. 11. Contour plots of density, kinematic viscosity, and molecular diffusivity as functions of mixture fraction for the LES calculations.

coflow (air), where $\Gamma_1(\xi_1 = 0, \xi_2 = 0) = 9.79 \times 10^{-6}$ m^2/s. Elsewhere in composition space, there is as much as 30% variation in Γ_1. For ethylene, Γ_2^e is in very good agreement to the numerically computed value at the composition of the jet (air and acetone), where $\Gamma_2(\xi_1 = 1, \xi_2 = 0) = 14.8 \times 10^{-6}$ m^2/s. The variation of Γ_2 in composition space is less than that of Γ_1, with a maximum variation of about 10%.

Contour plots of the density, molecular kinematic viscosity, and molecular diffusivities of both mixture fractions are shown in Figure 11 as functions of mixture fraction. The variation of each property in composition space is evident, with the molecular viscosity varying by as much as 80%.

B. Computational configuration

The system of equations described in Sec. IV A is solved on a cylindrical computational domain of size $54D \times 13.5D \times 2\pi$ in the axial, radial, and circumferential directions (with dimensions in the axial and radial directions equivalent to those in the RANS-PDF calculations). The equations are solved using a second-order accurate numerical method.[51] A sketch of the computational domain is shown in Figure 12. As illustrated in the figure, the domain begins at the jet exit plane and extends downstream in the axial direction.

Inflow boundary conditions for the central jet are provided from separate high-resolution LES calculations of a fully developed pipe flow at a Reynolds number of 14 300, based on the jet bulk velocity, diameter, and viscosity as in Table I. For the annulus stream, the same procedure is performed using an annular geometry, with the properties of the annulus stream in Table I. For the coflow, a laminar boundary condition is prescribed identical to that in the RANS-PDF calculations. At the other boundaries, convective boundary conditions are employed for scalar and velocity fields.

One important modeling difference is that the jet wall, whose width is reasonably large at $0.073D$, is instead modeled as having zero thickness; the dimensions of the jet width remain unchanged, and

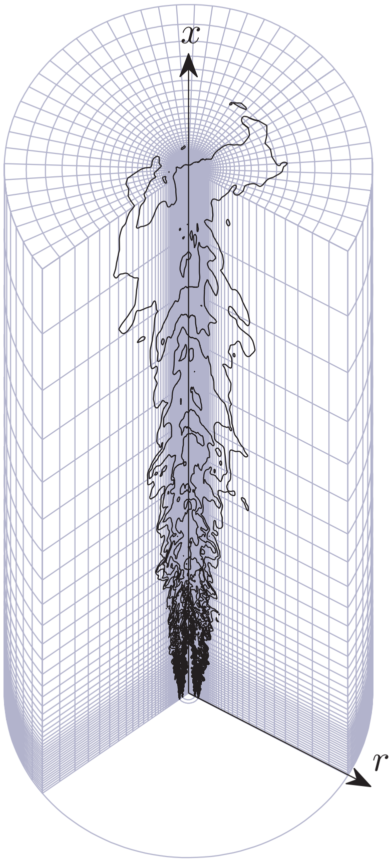

FIG. 12. Sketch of the LES domain. In the axial and radial directions, only one-eighth of the grid cells from grid G-D are shown. Contour lines of the resolved annulus mixture fraction are shown in the cutaway.

the effective inner radius of the annulus is decreased. This decision is made based on convergence studies performed in both geometries. In the calculations including the jet wall thickness, the calculations fail to reach satisfactory numerical convergence on all of the examined grid sizes. In the calculations with the infinitesimally thin jet wall, the calculations reach sufficient convergence of the mean fields on moderate grid sizes. This modeling assumption results in predictions of the annulus mixture fraction being slightly too large at some locations. However, in these calculations it is more desirable to have sufficient numerical convergence in light of the type of comparisons being made. The difference in the axial velocity mean and variance can be seen in Figure 2. There is clearly a larger bulk flow through the annulus which results in the larger annulus mixture fractions observed at some locations. The other differences in the RANS and LES boundary conditions are due to the effects of the turbulence modeling differences between the two sets of calculations.

In the LES calculations, the joint PDF of the resolved mixture fractions is computed at the same locations as in the RANS-PDF calculations. The resolved and modeled scalar dissipation rates for both mixture fractions are computed as in Eq. (8) using second-order central differences in both the two components (as performed in the experiment[36]) and in the full three components. Both the total conditional diffusion,

$$D_T = \langle (1/\bar{\rho})\, \nabla \left(\bar{\rho} \left(\widetilde{\Gamma} + \Gamma_T \right) \nabla \widetilde{\xi} \right) | \widetilde{\xi} = \hat{\xi} \rangle, \tag{12}$$

and the constant-property resolved conditional diffusion,

$$D_R = \langle \widetilde{\Gamma} \nabla^2 \widetilde{\xi} | \widetilde{\xi} = \hat{\xi} \rangle, \tag{13}$$

are computed at the same locations for both mixture fractions using second-order central differences, again in both two and three components. The calculations are run at a constant CFL number of 0.2

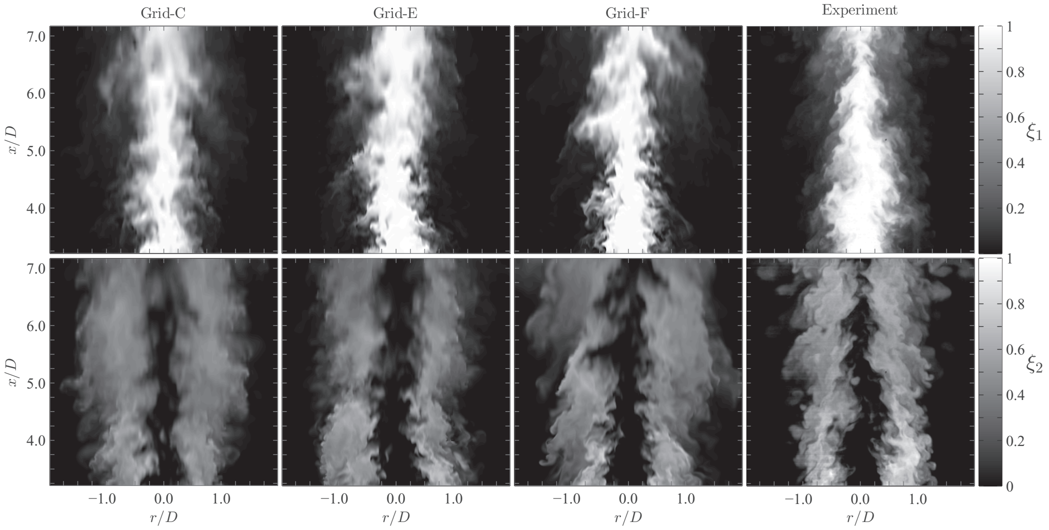

FIG. 13. Contour plots of instantaneous resolved mixture fractions of the jet (top plots) and pilot (bottom plots) in the LES convergence study and from experimental data.

and the statistics of interest are time-averaged over at least 10 flow-through times after a statistically stationary state is reached; a flow-through time is based on the jet bulk velocity and the entire extent of the domain in the axial direction.

C. Numerical accuracy

The LES solution depends strongly on the resolution with which it is computed. Therefore, it is important to quantify the extent to which the solution is resolved, and to understand how the resolution affects the statistics of interest. To examine the numerical accuracy of the calculations, a grid resolution study is conducted on six grids, named from Grid-A to Grid-F, whose sizes range from 0.5×10^6 cells to 33×10^6 cells. Contours of the instantaneous resolved jet and annulus mixture fractions are shown from calculations on three of the grids in Figure 13, alongside an instantaneous image obtained experimentally in Ref. 36.

While the large-scale features of the flow are similar among the three grids and the experimental data, there is a clear difference in the resolution of the small-scale features of the flow. On the finest grid, Grid-F, the resolution is similar to that of the experiment for the region near the jet exit plane (around $x/D = 3.5$), but farther downstream it is evident that even the finest grid does not fully resolve the small-scale structures observed at the experimental resolution. Figure 14 illustrates the large dependence of the resolved scalar dissipation rate (here for the annulus mixture fraction) on the grid resolution.

Each grid used in the LES calculations is a structured, tensor-product grid. The tensor-product grid here is created using a vector for each dimension (x, r, z) giving the grid coordinates in that dimension. The length of each vector for each dimension is equal to the number of grid nodes in that dimension. Each cell is then indexed by (i, j, k) for the (x, r, z) dimensions with the coordinates of the cell given by the ith entry of the vector for the x-dimension, the jth entry of the vector for the y-dimension, and the kth entry of the vector for the z-dimension. In the region of the near-field ($0 \leq x/D \leq 4.0$, $0 \leq r/D \leq 1.4$), the grid spacing is uniform. From the outer boundary of this region, the grid is stretched to each edge of the computational domain with a constant stretching ratio of 4% in each direction. Table V shows the size of each grid, along with the error in the resolved mixture fractions (ϵ_{M1} and ϵ_{M2}), the error in the resolved RMS (ϵ^R_{R1} and ϵ^R_{R2}), and the error in the total RMS (ϵ^T_{R1} and ϵ^T_{R2}). These errors are computed for each grid by taking the maximum value of the difference between the statistics on that grid, and the statistics on the most highly resolved grid

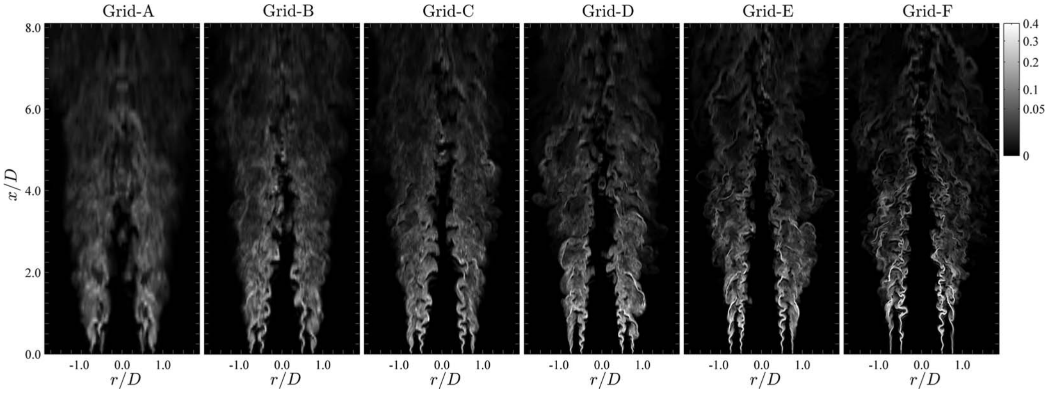

FIG. 14. Contour plots of instantaneous resolved scalar dissipation rate of the annulus mixture fractions for each grid used in the LES convergence study. Units are in s^{-1}.

within the region of interest ($3.29 \leq x/D \leq 6.99$). The convergence is relatively slow, and not till Grid-E do the statistics reach roughly the same numerical error as in the experiment, around 2%.

The results of the LES grid convergence study are summarized in Figure 15, where the radial profiles of time-averaged density-weighted mean and RMS statistics of both mixture fractions are shown for three grids and for the experimental data. The agreement between the most highly resolved LES calculations (Grid-F) and the experimental data is very good. The mean annulus mixture fraction is slightly overpredicted due to the thin-wall modeling assumption discussed in Sec. IV B. The total RMS on Grid-F is slightly overpredicted, mostly in the near-field around the jet-annulus mixing layer. This occurs due to both the modeling of the scalar dissipation rate and the high resolution requirements in the near-field of the jet. As the grid is refined, the statistics generally converge monotonically to the values on the finest grid. The total RMS decreases toward the resolved RMS as the grid is refined.

The results of the grid convergence study are further analyzed through Figures 16–19, which show statistics at various points as functions of the local grid resolution for all six grids, Grid-A to Grid-F, and the experimental data. The resolution, Δ, used in the plots is defined equivalently for the experimental data and calculations: in both cases, $\Delta = \sqrt{\Delta x^2 + \Delta r^2}$, where the local grid spacing (or image resolution) in the axial direction is Δx, and in the radial direction is Δr. This definition of Δ is used in these plots so that the experiments and calculations can be compared to one another with an equivalent definition for the resolution. It must be noted that the Δ defined here is not equal to the turbulence resolution scale used in the LES calculations (although they are closely related).

Figure 16 shows the mean resolved mixture fractions as a function of the grid resolution. These statistics are generally not very sensitive to the grid resolution beyond the most coarse grid, Grid-A. Besides the slight overprediction of the annulus mixture fraction, these statistics are all in good agreement with the experimental data for Grid-B and finer. The resolution of the calculations for Grid-F is higher than that of the experiments at $x/D = 3.29$; due to the grid stretching that occurs

TABLE V. Grid sizes (number of cells in x, r, and θ, and total number of cells in millions, n_T) and errors in the mixture fraction statistics (resolved means, RMS of resolved fields, total RMS) from convergence tests of the LES-PDF calculations.

Grid name	n_x	n_r	n_θ	n_T	ϵ_{M1}	ϵ_{M2}	ϵ^R_{R1}	ϵ^R_{R2}	ϵ^T_{R1}	ϵ^T_{R2}
G-A	128	128	32	0.524	0.132	0.087	0.151	0.124	0.073	0.058
G-B	192	192	96	1.77	0.073	0.075	0.098	0.102	0.072	0.041
G-C	256	256	64	4.19	0.053	0.060	0.064	0.066	0.062	0.032
G-D	320	320	80	8.19	0.022	0.034	0.029	0.030	0.044	0.020
G-E	384	384	96	14.2	0.008	0.010	0.025	0.017	0.019	0.012
G-F	512	512	128	33.6	...	...	...	...	...	...

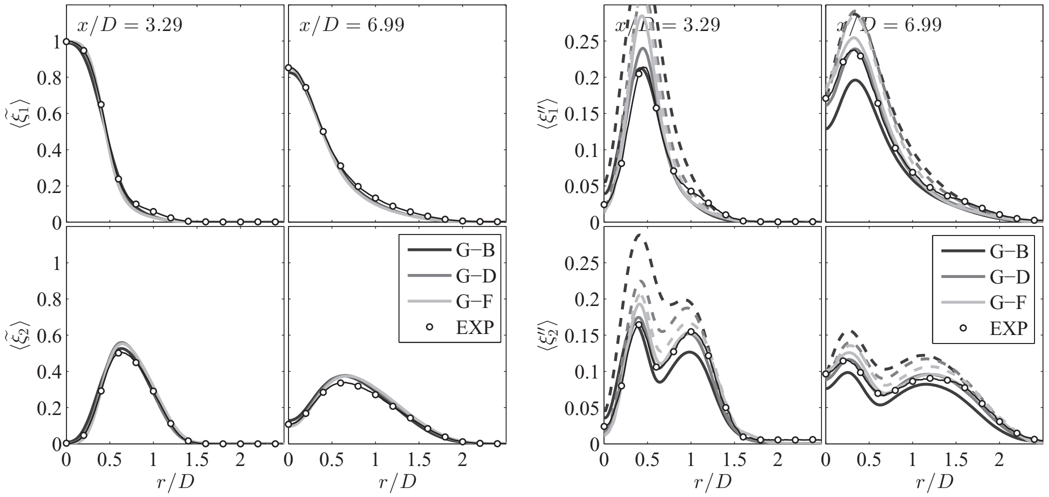

(a)

(b)

FIG. 15. Radial profiles of time-averaged mass-weighted mean (a) and RMS (b) mixture fractions in the LES grid convergence study. Dark line: Grid G-B; dark gray line: Grid G-D; light gray line: Grid G-F; solid lines: resolved statistics; dashed lines: total (resolved plus modeled) statistics; circles: experimental data.[36]

beyond *x*/*D* = 4, the calculations on Grid-F are at a lower resolution than the experiments farther downstream at *x*/*D* = 6.99. These quantitative assessments of the resolution are consistent with the qualitative comparisons of the instantaneous resolved fields in Figure 13.

The next figures, Figures 17–18, show the RMS of the jet and annulus mixture fractions, respectively. As the grid is refined, the portion of the RMS which is modeled approaches zero, and the total RMS is nearly equal to the resolved portion of the RMS. As observed in Figure 15, the RMS of the jet mixture fraction is overpredicted at the jet-annulus mixing layer, (*x*/*D*, *r*/*D*) = (3.29, 0.40). At this location, the modeled portion of the RMS is about 10% of the total RMS and the total RMS has changed little between the three finest grids. Therefore, this overprediction in the RMS

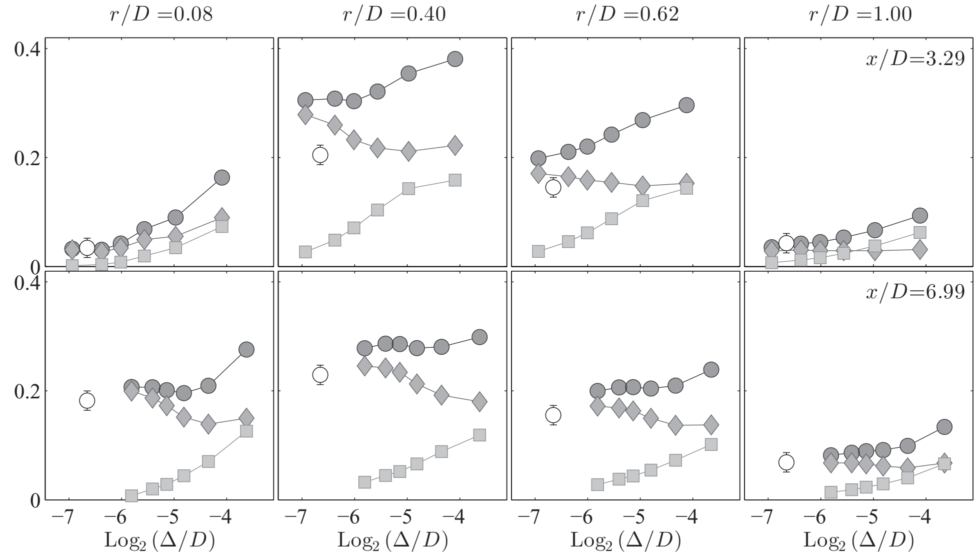

FIG. 16. Convergence of the time-averaged density-weighted mean resolved mixture fractions at eight locations in the flow. Circles: jet mixture fraction; diamonds: annulus mixture fraction; solid symbols: LES calculations; open symbols: experimental data.[36]

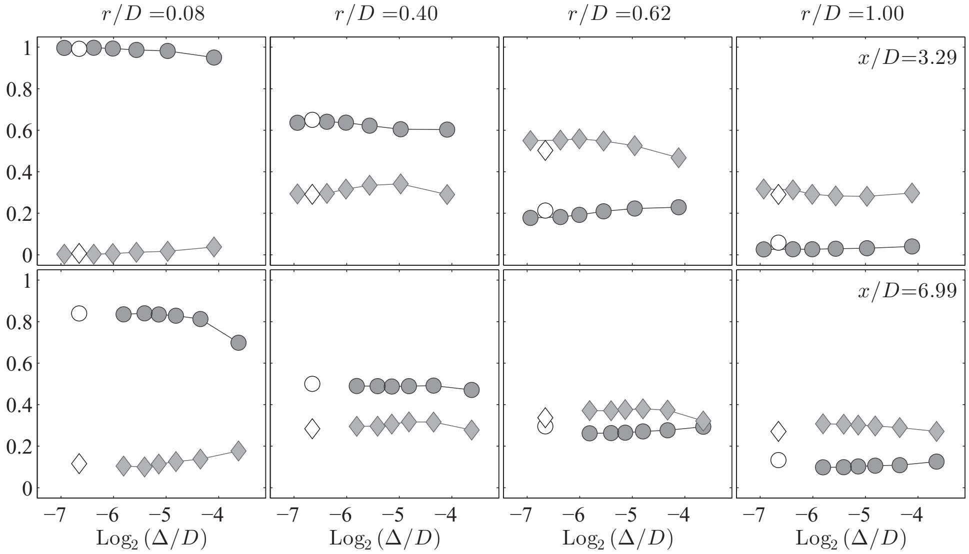

FIG. 17. Convergence of the time-averaged density-weighted RMS jet mixture fraction at eight locations in the flow. Circles: total RMS; diamonds: resolved RMS; squares: modeled RMS; solid symbols: LES calculations; open symbols: experimental data.[36]

is not necessarily caused by under-resolution. Modeling errors which can affect the calculations in the near-field, such as the modeling of the inflow boundary conditions, are also a likely cause of this overprediction. Farther downstream at $x/D = 6.99$, the agreement between the RMS of the jet mixture fraction in the calculations and the experiments is better, even though the resolution in the calculations is comparatively lower. This shows that the LES is performing well in this region of the flow. For the RMS of the annulus mixture fraction in Figure 18, the agreement with the experimental data is slightly better and indicates convergence toward the experimentally measured values. In general, the convergence of the RMS statistics is slower than that of the mean statistics, with reasonable convergence being achieved not till Grid-D or Grid-E.

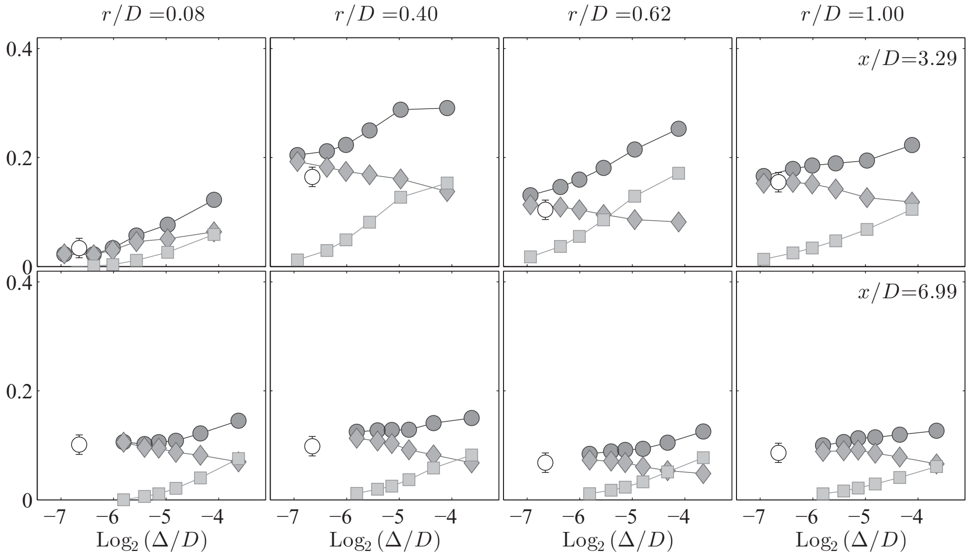

FIG. 18. Convergence of the time-averaged density-weighted RMS annulus mixture fraction at eight locations in the flow. Circles: total RMS; diamonds: resolved RMS; squares: modeled RMS; solid symbols: LES calculations; open symbols: experimental data.[36]

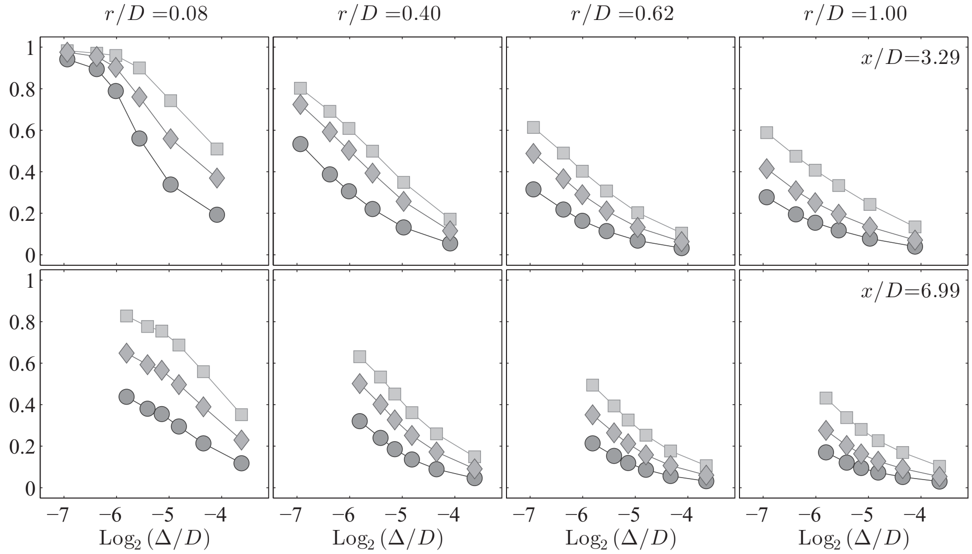

FIG. 19. Convergence of the time-averaged molecular viscosity and molecular diffusivities as fractions of the total (molecular plus turbulent) viscosity and diffusivity, plotted as functions of the grid length scale. Squares: molecular viscosity; circles: molecular diffusivity of acetone; diamonds: molecular diffusivity of ethylene.

Figure 19 shows the time-averaged molecular viscosity and molecular diffusivities as fractions of the total viscosity and diffusivity. At the centerline of the inflow boundary, the Kolmogorov scale, η, is estimated to be 63 μm (equivalent to $\log_2(\eta/D) = -6.5$ on the horizontal axis of Figure 19) in the experimental work[36] based on extrapolation from experimental data. This is reasonably close to the grid resolution at which the turbulent diffusivity goes to zero at a location of $(x/D, r/D) = (3.29, 0.08)$. Classical scaling of the flow's smallest length scales based on the Reynolds number of the jet, $\eta/D \sim Re^{-3/4}$, yields η on the order of 4.2 μm (or $\log_2(\eta/D) \sim -10.4$ on the horizontal axis of Figure 19). This is far smaller than any of the resolution scales encountered in either the experiment or the calculations; based on linear extrapolation from the grid resolution study, it appears to be a reasonable approximation around $r/D = 0.62$ and $r/D = 1.00$, near the middle of the jet-annulus and annulus-coflow mixing layers.

Figure 19, in conjunction with Figures 16–18, conveys the efficacy of LES: with less than 20% of the molecular diffusivity resolved, accurate calculations of the mean statistics are achieved; with less than 40% of the molecular diffusivity resolved, accurate calculations of the RMS statistics are achieved; accurate calculations of these statistics are achieved with a grid resolution scale more than 10 times greater than the order estimate of the smallest Kolmogorov scales.

D. Scalar dissipation rate and conditional diffusion

As mentioned in Sec. II, one of the highlights of the experimental work is performing the challenging measurements of the scalar dissipation rate and conditional diffusion. In the experiment, the resolved scalar dissipation rate, from Eq. (9), is computed in two-dimensions from the planar imaging measurements. This same quantity is also calculated from the LES as mentioned in Sec. IV B. Figure 20 compares this quantity for calculations on all six LES grids and the experimental measurements. It is clear from the figure that this quantity is extremely dependent on the grid resolution, which is expected since Eq. (9) depends on the square of gradient fields. The form of $\widetilde{\chi}_R$ is qualitatively the same in the experiments and in the calculations; for the jet mixture fraction, there is a peak in the scalar dissipation rate near the jet-annulus mixing layer; for the annulus mixture fraction, there are two peaks, corresponding to the jet-annulus and annulus-coflow mixing layers.

The differences that occur between the experimental measurements and the calculations on Grid-F are attributed to a number of factors. These factors include:

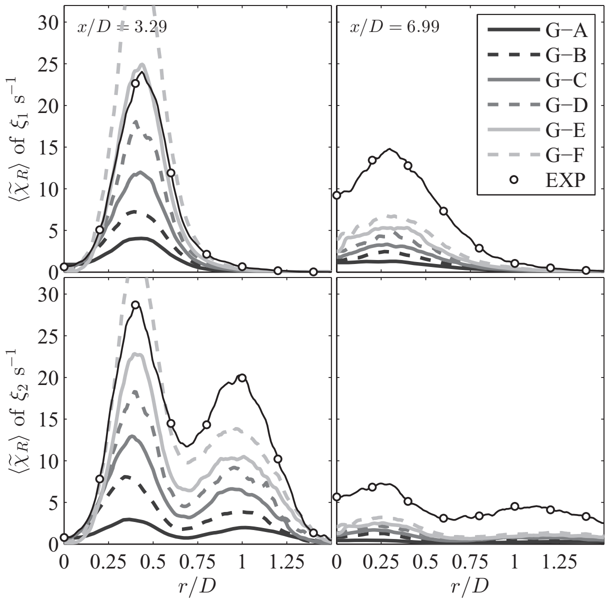

FIG. 20. Radial profiles of the time-averaged two-dimensional scalar dissipation rates of resolved jet (top) and annulus (bottom) mixture fractions: Solid and dashed lines: LES calculations on all six grids; open circles: experimental measurements.[36]

1. *Under-resolution of the calculations* – Keeping in mind the resolution quality as discussed in Sec. IV C, at $x/D = 6.99$, the resolution scale of the calculations on Grid-F is more coarse than that of the experiments by a factor of about two. The scalar dissipation rate here is under-estimated in the calculations.
2. *Under-resolution of the experimental measurements* – At $x/D = 3.29$, where the scalar dissipation rate in the experiments is less than that of the LES on Grid-F, the resolution scale of the calculations on Grid-F is finer than that of the experiments by a factor of 1.4.
3. *Additional numerical procedures undertaken in the experiments* – In the experiments, high order differences are used to calculate the scalar dissipation (tenth-order versus second-order), conditional sampling techniques are used to improve the resolution, and noise-correction procedures are performed on the experimental data. Based on the sensitivity of this quantity to the grid resolution, this factor is not a likely cause of the differences observed.
4. *Experimental noise* – The experimental measurement noise is clearly evident from the non-realizable values of mixture fraction in the plots of conditional diffusion later in this section. The contribution of the experimental noise to the differences observed here is most likely small, as Ref. 36 has shown the effects of noise-reduction applied to the measurements and it is far less than the differences observed here.

Figure 21 shows total scalar dissipation rate, $\widetilde{\chi}$, from Eq. (8) and from the LES calculations. Compared to $\widetilde{\chi}_R$, there is much less sensitivity of $\widetilde{\chi}$ to the grid resolution. The modeled portion of the total scalar dissipation rate is large; even on Grid-F, as much as 90% of the total dissipation is from the model. The time-averaged scalar dissipation rate from the RANS-PDF equations is modeled here using a commonly applied closure in RANS methods of

$$\langle \chi \rangle = C_\phi \langle \omega \rangle V_\xi^T, \tag{14}$$

where $\langle \omega \rangle$ is the time-averaged turbulence frequency, and V_ξ^T is the variance of the mixture fraction, is also shown in Figure 21. Both models for the total scalar dissipation rate are considerably larger than the values measured experimentally. Along with the observation from Figure 20 that the resolved portion of the scalar dissipation rate is still sensitive to the grid resolution on the finest grid and giving no indication of convergence, Figure 21 suggests that the scalar dissipation rates measured experimentally are not fully resolved. Even with the fine resolution used in the experiments,

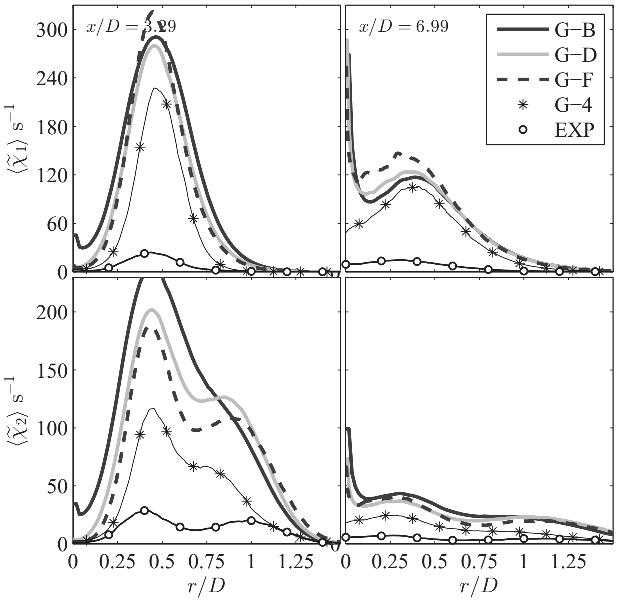

FIG. 21. Radial profiles of the time-averaged total scalar dissipation rates of the jet (top) and annulus (bottom) mixture fractions: Solid and dashed lines: LES calculations on three grids; stars: RANS-PDF calculations; open circles: experimental measurements.[36]

Figures 20 and 21 indicate that assessments of these measurements need to take into account the resolution at which the measurements are made.

A second observation from Figure 21 is the very sharp peak in the total scalar dissipation rate from the LES calculations at the centerline, $r/D = 0$. This is observed when using both the dynamic model[54,55] and the algebraic model[56] (not shown) for the turbulent viscosity, ν_T. An inspection of each calculation shows that this behavior occurs due to the quantity Γ_T/Δ^2. This demonstrates the need for improved models in LES for ν_T (which, in this study, is directly proportional to Γ_T by the turbulent Schmidt number) or the scalar dissipation rate. As this observed behavior is most likely a numerical artifact caused by the very small filter widths at the centerline, an alternate definition of the filter width used in the model for the scalar dissipation is a potential remedy.

The LES study is concluded by presenting the calculations of the conditional diffusion and comparing these to the experimentally measured values. In the experimental work, the constant-property resolved conditional diffusion from Eq. (13) is computed in the two-dimensional (x, r) plane. This same measurement is made in the LES calculations (although using only second-order central differences to calculate the gradients, instead of tenth-order, as in the experiment). The results are shown in Figure 22 for three different LES grids at one location, $(x/D, r/D) = (3.29, 0.536)$. In the previous figures of the conditional diffusion (Figures 7 and 8), only the magnitude and streamlines are shown; here contour plots show each component of the conditional diffusion. This allows a more direct comparison to be made regarding the form of the conditional diffusion in composition space.

As expected, there is large grid dependency in this quantity as well. For all grids, the qualitative form of the conditional diffusion is very similar; generally only the magnitude appears to be strongly influenced by the grid resolution. Note that the color scale in Figure 22 is different on the left two plots for the more coarse grids. On the finest grid, Grid-F, there is reasonable quantitative agreement in the values of conditional diffusion with the experimentally measured values. At some locations in composition space at which there are large differences between the experimental values and those computed on Grid-F, the measured composition is actually non-realizable (i.e., a sum of mixture fractions greater than unity); the only reason for a value of the conditional diffusion existing at these compositions is due to measurement noise. It is conceivable then, that at least some of the differences between the measurements of the conditional diffusion and the LES calculations on Grid-F are due to measurement error. In general, the form of the conditional diffusion observed in

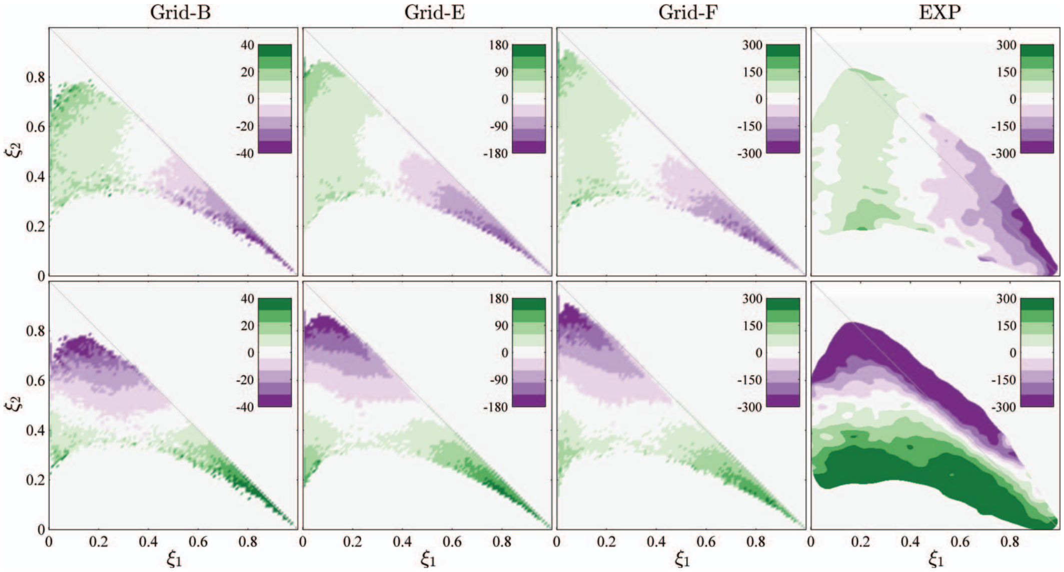

FIG. 22. Contour plots of the constant-property resolved conditional diffusion, $D_R=\langle\tilde{\Gamma}\nabla^2\tilde{\xi}|\tilde{\xi}=\hat{\xi}\rangle$, from LES calculations on three grid (leftmost three columns) and the experimentally measured conditional diffusion[36] (right column), for the jet (top) and annulus (bottom) mixture fractions, i.e., $\langle\tilde{\Gamma}\nabla^2\tilde{\xi}_1|\tilde{\xi}=\hat{\xi}\rangle$ and $\langle\tilde{\Gamma}\nabla^2\tilde{\xi}_2|\tilde{\xi}=\hat{\xi}\rangle$, respectively. The units are s^{-1}, and the location is $(x/D, r/D) = (3.29, 0.536)$.

the LES calculations here is very similar to that observed in the temporally evolving three-stream mixing layer studied both with DNS[39] and PDF[40] methods.

As Figure 22 examined only the resolved, constant-property, two-dimensional conditional diffusion, Figure 23 shows the total conditional diffusion, from Eq. (12) in all three dimensions with the same color scale on each plot. It is found from the calculations that the largest contribution to the differences between the values in Figure 22 and those in Figure 23 is the addition of the modeled portion of the conditional diffusion (by adding the turbulent diffusivity); the additional third-dimensional component and the inclusion of the variable properties (both of which are not considered in the experimental measurements) account for a difference of only about 10% at most.

There is much less sensitivity of the total conditional diffusion to the grid resolution since the modeled portion is accounted for. This allows even the coarse grids to yield a magnitude of the conditional diffusion which is close to the experimental measurement. Due to the form of the turbulent diffusivity, the structure of the conditional diffusion in composition space changes slightly from that of the resolved conditional diffusion; for example, in the region of the jet composition, the turbulent diffusivity is large, which results in a calculation of the conditional diffusion being considerably larger than what is measured experimentally. It is not immediately clear whether the addition of the turbulent diffusivity results in inaccurate total conditional diffusion in the LES calculations due to its modeling, or if the experimental measurements (which do not consider any turbulent diffusivity because they only contain the resolved portion of the conditional diffusion) are under-resolved. The results from Figures 20 and 21 suggest the latter is more responsible, but more conclusive tests must be performed before concluding so.

V. LES-PDF CALCULATIONS

A. LES-PDF methodology

The LES-PDF methodology, which combines many of the advantages of LES (discussed in Sec. IV) with the advantages of the PDF method (discussed in Sec. I), is next applied to this non-reacting flow to study the modeling of mixing in LES-PDF. The LES-PDF methodology involves a hybrid finite-volume and particle solver. The finite-volume solver in this case is LES, and solves the

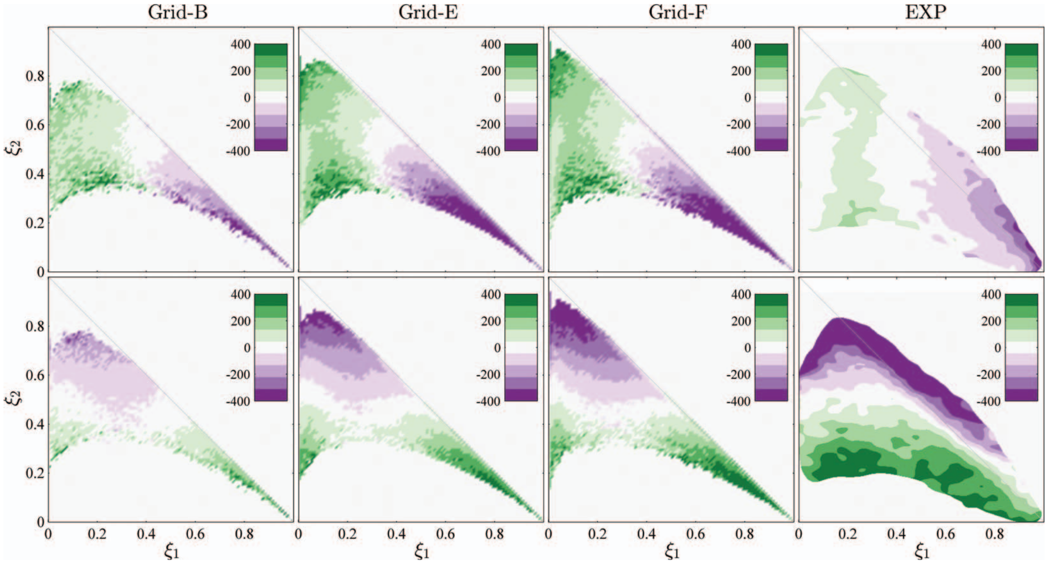

FIG. 23. Contour plots of the total conditional diffusion, $D_T = \langle (1/\bar{\rho})\nabla\left(\bar{\rho}\left(\widetilde{\Gamma}+\Gamma_T\right)\nabla\widetilde{\xi}\right)|\widetilde{\xi}=\hat{\xi}\rangle$, from LES calculations on three grid (leftmost three columns) and the experimentally measured conditional diffusion[36] (right column), for the jet (top) and annulus (bottom) mixture fractions, i.e., $\langle\tilde{\Gamma}\nabla^2\xi_1|\tilde{\xi}=\hat{\xi}\rangle$ and $\langle\tilde{\Gamma}\nabla^2\xi_2|\tilde{\xi}=\hat{\xi}\rangle$, respectively. The units are s^{-1}, and the location is $(x/D, r/D) = (3.29, 0.536)$.

same equations as described in Sec. IV A, except for the density equation. The density in the LES is computed from the particle solver through the transported specific volume method. In the particle solver, particles evolve in position according to

$$d\mathbf{X}^*(t) = \left(\widetilde{\mathbf{U}} + \frac{1}{\bar{\rho}}\nabla\left(\bar{\rho}\Gamma_R\right)\right)^* dt + \sqrt{2\Gamma_R^*}d\mathbf{W} \tag{15}$$

(where the * symbols refer to Lagrangian quantities at particle locations) and in composition as

$$d\phi^*(t) = -\Omega_M^*\left(\phi^* - \tilde{\phi}^*\right)dt + \left(\frac{1}{\bar{\rho}}\nabla\cdot\left(\bar{\rho}\Gamma_M\nabla\tilde{\phi}\right)\right)^* dt, \tag{16}$$

where Ω_M, the mixing frequency, is defined as

$$\Omega_M = C_M\left(\frac{\Gamma_M + \Gamma_R}{\Delta^2}\right). \tag{17}$$

The terms Γ_R and Γ_M represent the diffusivities for the random walk and the mean drift, respectively. Typically, the diffusivity for the random walk, Γ_R, is taken to be equal to the turbulent diffusivity, Γ_T, while the diffusivity for the mean drift, Γ_M, is taken be equal to the resolved molecular diffusivity, $\tilde{\Gamma}$. The position equation, Eq. (15), is solved with second-order accuracy in space and time.[60] The implementation of molecular diffusion in Eq. (16)[61,62] is unique in that it yields no spurious production of variance from molecular diffusion, and it can include the effects of differential diffusion. The first term in Eq. (16) represents an IEM-like model, relaxing the composition toward the cell mean.

The mass-weighted LES PDF of the composition is denoted as $\tilde{f}_\phi(\psi;\mathbf{X},t)$, where ψ is a sample-space variable for the composition. Equations (15)–(17) correspond to an equation for the evolution of the PDF, $\tilde{f}_\phi$, as

$$\begin{aligned}\frac{\partial\bar{\rho}\tilde{f}_\phi}{\partial t} + \frac{\partial}{\partial x_j}\left(\bar{\rho}\tilde{f}_\phi\widetilde{U}_j\right) &= \frac{\partial}{\partial x_j}\left(\bar{\rho}\Gamma_R\frac{\partial}{\partial x_j}\tilde{f}_\phi\right)\\ &\quad + \frac{\partial}{\partial\psi}\left(\bar{\rho}\tilde{f}_\phi\Omega_M\left(\psi - \widetilde{\phi}\right)\right) - \frac{\partial}{\partial\psi}\left(\tilde{f}_\phi\frac{\partial}{\partial x_j}\left(\bar{\rho}\Gamma_M\frac{\partial\widetilde{\phi}}{\partial x_j}\right)\right).\end{aligned} \tag{18}$$

Taking the first moment of Eq. (18), the transport equation for the resolved composition is

$$\frac{\partial \bar{\rho}\widetilde{\phi}}{\partial t} + \frac{\partial \bar{\rho}\widetilde{U}_j\widetilde{\phi}}{\partial x_j} = \frac{\partial}{\partial x_j}\left(\bar{\rho}\left(\Gamma_R + \Gamma_M\right)\frac{\partial \widetilde{\phi}}{\partial x_j}\right). \tag{19}$$

Similarly, taking the second moment of Eq. (18) gives the transport equation for the resolved square of the composition to be

$$\frac{\partial \bar{\rho}\widetilde{\phi^2}}{\partial t} + \frac{\partial \bar{\rho}\widetilde{U}_j\widetilde{\phi^2}}{\partial x_j} = \frac{\partial}{\partial x_j}\left(\bar{\rho}\Gamma_R\frac{\partial \widetilde{\phi^2}}{\partial x_j}\right) + 2\widetilde{\phi}\frac{\partial}{\partial x_j}\left(\bar{\rho}\Gamma_M\frac{\partial \widetilde{\phi}}{\partial x_j}\right) - 2\bar{\rho}\Omega_M\left(\widetilde{\phi^2} - \left(\widetilde{\phi}\right)^2\right). \tag{20}$$

The transport equation for the modeled variance, $V_\phi = \widetilde{\phi^2} - \left(\widetilde{\phi}\right)^2$, is obtained from Eqs. (19) and (20), and it is

$$\frac{\partial \bar{\rho}V_\phi}{\partial t} + \frac{\partial \bar{\rho}\widetilde{U}_j V_\phi}{\partial x_j} = \frac{\partial}{\partial x_j}\left(\bar{\rho}\Gamma_R\frac{\partial V_\phi}{\partial x_j}\right) - 2\bar{\rho}\Omega_M V_\phi + 2\bar{\rho}\Gamma_R\frac{\partial \widetilde{\phi}}{\partial x_j}\frac{\partial \widetilde{\phi}}{\partial x_j}. \tag{21}$$

In this work, the diffusivities Γ_R and Γ_M are related to the turbulent diffusivity, Γ_T, and the molecular diffusivity, $\widetilde{\Gamma}$, through the model constant β ($0 \le \beta \le 1$) as

$$\Gamma_R = \Gamma_T - \beta\Gamma_T \tag{22}$$

and

$$\Gamma_M = \widetilde{\Gamma} + \beta\Gamma_T. \tag{23}$$

With these specifications, the transport equation for the resolved composition (Eq. (19)) takes the standard form

$$\frac{\partial \bar{\rho}\widetilde{\phi}}{\partial t} + \frac{\partial \bar{\rho}\widetilde{U}_j\widetilde{\phi}}{\partial x_j} = \frac{\partial}{\partial x_j}\left(\bar{\rho}\left(\widetilde{\Gamma} + \Gamma_T\right)\frac{\partial \widetilde{\phi}}{\partial x_j}\right), \tag{24}$$

independent of the value of β; and the resolved variance equation (Eq. (21)) can be written

$$\frac{\partial \bar{\rho}V_\phi}{\partial t} + \frac{\partial \bar{\rho}\widetilde{U}_j V_\phi}{\partial x_j} = \frac{\partial}{\partial x_j}\left(\bar{\rho}\Gamma_R\frac{\partial V_\phi}{\partial x_j}\right) + 2\bar{\rho}\Gamma_T\frac{\partial \widetilde{\phi}}{\partial x_j}\frac{\partial \widetilde{\phi}}{\partial x_j} - \bar{\rho}\widetilde{\chi}_M, \tag{25}$$

where $\widetilde{\chi}_M$ is the implied model for the scalar dissipation

$$\widetilde{\chi}_M = 2\Omega_M V_\phi + 2\beta\Gamma_T\frac{\partial \widetilde{\phi}}{\partial x_j}\frac{\partial \widetilde{\phi}}{\partial x_j}. \tag{26}$$

The value of β affects the diffusion coefficient, Γ_R, but more importantly (for $\beta > 0$) it adds a contribution to the modeled dissipation, which is β times the production of V_ϕ. In previous LES-PDF studies using a similar methodology,[63–65] the value of β is simply zero, so this "production" contribution to the modeled dissipation is absent. The "production" contribution to $\widetilde{\chi}_M$ has been used in many previous LES studies (see, e.g., Ref. 66), but this is the first time that it has been proposed and used in LES-PDF. We refer to the last term in Eq. (26) as the *attenuation of variance production* model for (part of) the scalar dissipation, since in Eq. (25) it has the overall effect of attenuating the production term by the factor β. Similarly, we refer to Eq. (15) as the *attenuated random walk* implementation of this model, since the diffusivity involved, Γ_R, is the turbulent diffusivity attenuated by the factor β.

B. Numerical accuracy

The computational configuration of the LES-PDF calculations is identical to that of the LES calculations, described in Sec. IV B. The base case calculations use 20 particles per cell, a value of $C_M = 5$, and the standard value of $\beta = 0$. Convergence studies on the number of particles per cell shows little sensitivity compared to the sensitivity observed from the effect of the grid resolution. The numerical error due to the grid resolution is investigated through calculations on grids A–C from Table V.

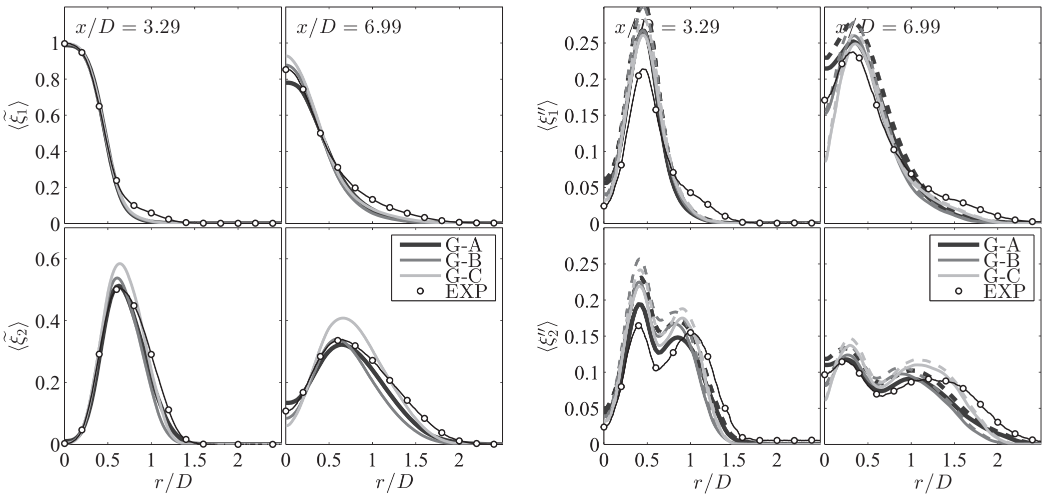

(a)

(b)

FIG. 24. Radial profiles of time-averaged mass-weighted mean (a) and RMS (b) mixture fractions in the LES-PDF grid convergence study. Dark line: Grid G-A; dark gray line: Grid G-B; light gray line: Grid G-C. solid lines: resolved statistics; dashed lines: total statistics; circles: experimental data.[36]

The radial profiles of the time-averaged mass-weighted mean and RMS statistics from the LES-PDF grid convergence study are shown in Figure 24. On the coarse grids, the LES-PDF solution is generally more accurate (compared to the most numerically accurate LES calculation) than that of the corresponding LES calculation, and convergence in most regions of the flow is achieved at relatively more coarse grids. One exception is the area of the annulus-coflow mixing, near $r/D = 1.5$. The calculations in this region are found to be more sensitive to numerical errors from the velocity and turbulent diffusivity interpolation. The results presented in Figure 24 employed second-order interpolation schemes for both the velocity and turbulent diffusivity. When larger time steps and/or first-order interpolation schemes were used, the predictions in this annulus-coflow regions were worse, whereas the rest of the domain was found to be less affected.

Joint PDFs are sampled from the particles in the LES-PDF calculations using the same procedure described in Sec. III B. Figure 25 shows the joint PDF at a location of $(x/D, r/D) = (6.99, 0.635)$ for LES-PDF calculations grids A–C. The quantitative agreement with the experimental measurements is reasonable for all three grid resolutions. There is a very large improvement in the accuracy compared to the previously discussed RANS-PDF calculations in Sec. III D using the IEM and EMST mixing models, and a small improvement from the RANS-PDF calculations with MC.

Also shown in Figure 25 is the conditional diffusion from the LES-PDF calculations. The differences between the experimental measurements and the calculations can be explained by the observations made in Sec. IV D and an explanation of the terms in Eq. (16). The right-hand side of Eq. (16) is composed of two terms: first, the molecular mixing term, and second, the molecular transport term. The resolved conditional diffusion (which corresponds to molecular transport) is small compared to the total conditional diffusion, especially on the coarse grids examined in this section. The contribution of both molecular mixing and molecular transport have been examined in this study; on these grids, molecular transport generally contributes little more than 10% to the total conditional diffusion. As seen in Sec. IV D, the addition of the turbulent diffusivity to the calculation of the conditional diffusion results in a departure from the experimentally measured values; similarly here, the addition of the molecular mixing into the calculation of the conditional diffusion shows a difference in form to the measurements. Whether this difference is due to the form of the turbulent diffusivity and the mixing model, the resolution of the measurements, or both is not immediately clear.

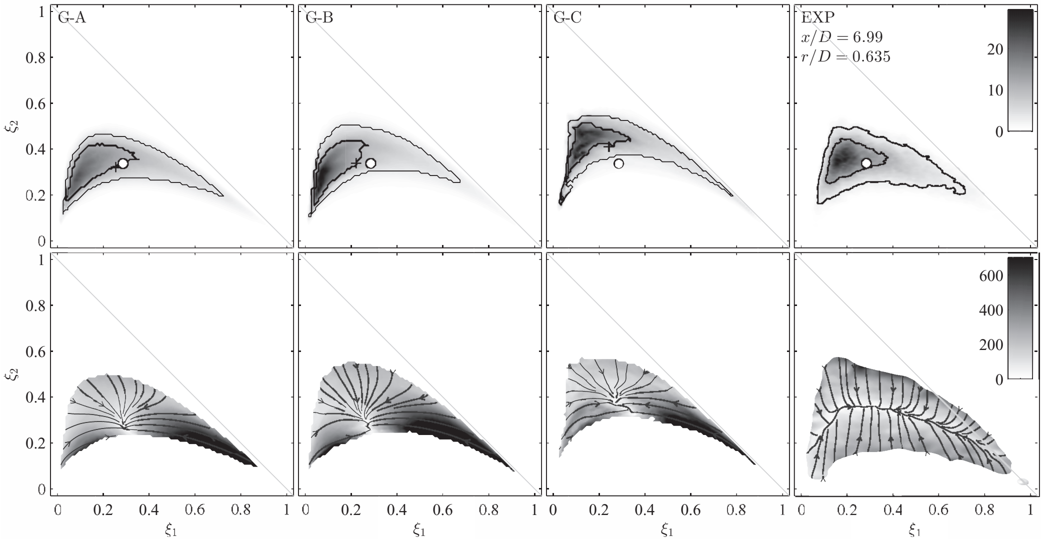

FIG. 25. Contour plots of the joint PDF of mixture fractions (top) and the magnitude of conditional diffusion (bottom) at (x/D, r/D) = (6.99, 0.635) from the experimental data[36] (right) and LES-PDF calculations on different grids, from left to right: G-A, G-B, and G-C. The circle is the experimental mean, and the plus sign is the mean from the PDF calculation. In the top plots, the two solid lines are isocontours which enclose regions with probability 0.5 and 0.9. In the lower plots, the lines with arrows are streamlines, everywhere parallel to the conditional diffusion vector.

C. Effect of the mixing models

Since the mixing models are the primary source of modeling uncertainty in these calculations, it is imperative to investigate the sensitivity of the calculations to the model constant C_M (which is analogous to, but not equivalent to, the model constant C_ϕ in the RANS-PDF calculations). Most other calculations using this LES-PDF methodology use values of C_M around 4–5,[64,65] and values of $C_M = \{1, 2, 5, 10\}$ are investigated here.

Figure 26 shows radial profiles of the mean and RMS statistics for different values of C_M on Grid-B. There is very little effect of C_M on the mean statistics. This result is expected with the composition PDF method, since C_M only affects the mean through the feedback of the density into the velocity field, and in this flow the variation in density is small. The effect of C_M on the RMS is much stronger; the resolved RMS slightly decreases as C_M increases, and the total RMS decreases significantly as C_M increases. This is the expected behavior since increasing C_M directly increases the dissipation of the modeled variance as shown in Eq. (21). The calculations shown in Figure 26 employ the algebraic SGS model,[56] which was observed here to yield larger scalar variance than the dynamic model,[54,55] which was used for the calculations presented in Figure 24.

The effect of C_M on the joint PDF is shown in Figure 27. As C_M increases, the variance in composition space can clearly be observed to decrease, as the joint PDF comes closer together. In fact, with very small values of C_M, the joint PDF is bimodal at the location shown, which is clearly different from the experimental measurements. The best agreement with the experimentally measured joint PDF is achieved with C_M of 5 (not shown in Figure 27) or 10, and there is indeed a large sensitivity of the joint PDFs to the value of C_M. Increasing C_M directly increases the conditional diffusion, and this is also clear from Figure 27.

In the base case LES-PDF calculations with a value of $\beta = 0$ and the mixing frequency, Ω_M, modeled according to Eq. (17), the modeled scalar dissipation rate takes the form

$$\widetilde{\chi}_M = 2C_M \left(\frac{\widetilde{\Gamma} + \Gamma_T}{\Delta^2} \right) V_\phi. \tag{27}$$

The modeled scalar dissipation rate in LES-PDF from Eq. (27) is consistent with that of the LES (the last term in Eq. (8)) when $2C_M = C$ and $C_D = 1$. It is noted that in this study, a value of $C_D = 2$

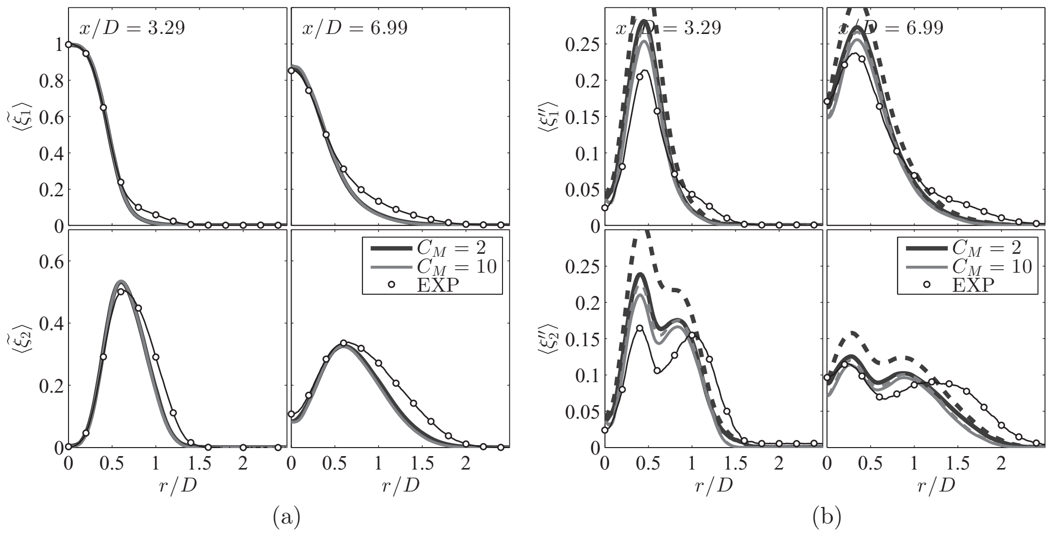

FIG. 26. Radial profiles of time-averaged mass-weighted mean (a) and RMS (b) mixture fractions in the LES-PDF calculations for different values of C_M. Dark line: $C_M = 2$; light line: $C_M = 10$; solid lines: resolved statistics; dashed lines: total statistics; circles: experimental data.[36]

is used, but this difference has very little affect on the modeled scalar dissipation rate since, in most regions investigated in this flow, the turbulent diffusivity is substantially greater than the molecular diffusivity (typically by a factor of 10–100 on the coarse grids). The LES-PDF study of C_M shows that the value of C_M yielding the best agreement with the experimental data is around 5 or 10, which suggests the use of larger values of C than used in the LES study here ($C = 2$ in the base case). This is demonstrated in Figure 28, which shows radial profiles of the mean modeled scalar dissipation rate for the LES calculations, and LES-PDF calculations with $C_M = 1$ and $C_M = 5$. As expected, there is close agreement in the modeled scalar dissipation rate among the LES calculations on Grid-A and

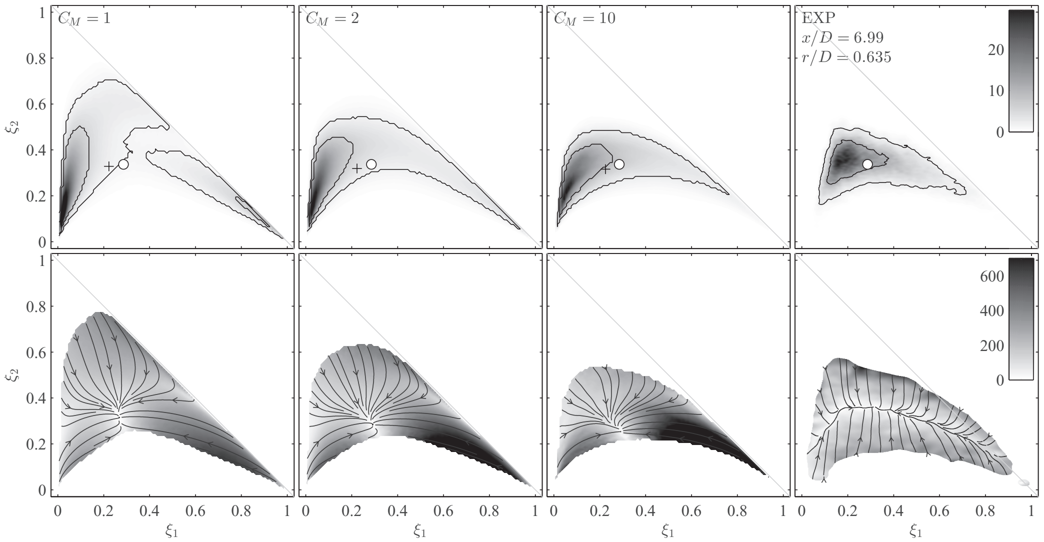

FIG. 27. Contour plots of the joint PDF of mixture fractions (top) and the magnitude of conditional diffusion (bottom) at $(x/D, r/D) = (6.99, 0.635)$ from the experimental data[36] (right) and LES-PDF calculations on grid G-B using different values of C_M, from left to right: 1, 2, and 10. The circle is the experimental mean, and the plus sign is the mean from the PDF calculation. In the top plots, the two solid lines are isocontours which enclose regions with probability 0.5 and 0.9. In the lower plots, the lines with arrows are streamlines, everywhere parallel to the conditional diffusion vector.

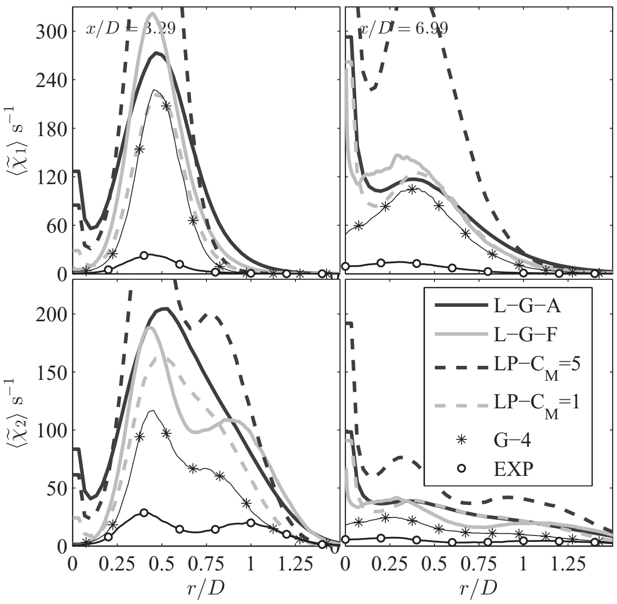

FIG. 28. Radial profiles of time-averaged mass-weighted mean total modeled scalar dissipation rate for the jet (top) and annulus (bottom) mixture fractions from different calculations. Solid dark line: LES on Grid-A; solid light line: LES on Grid-F; dashed dark line: LES-PDF on Grid-A with $C_M = 5$; dashed light line: LES-PDF on Grid-A with $C_M = 1$; stars: RANS-PDF; circles: experimental data.[36]

the LES-PDF calculations on Grid-A with $C_M = 1$, where $2C_M = C$. The agreement between these calculations is very good at $x/D = 6.99$, but slightly worse nearer the jet exit plane at $x/D = 3.29$, where the error from the time-stepping in LES-PDF is larger. The effect of C_M on the modeled scalar dissipation rate is not entirely obvious from Eq. (27). The modeled scalar dissipation rate, $\widetilde{\chi}_M$, is proportional to C_M, but the value of C_M also affects the modeled variance, V_ϕ. As shown in Figure 28, as C_M increases, the modeled variance decreases, but not enough to counter the direct effect of C_M on the modeled scalar dissipation rate. The larger dissipation rates observed with $C_M = 5$ yield even greater departures from the relatively small values measured experimentally. The LES-PDF calculations with $C_M = 5$ demonstrate that even larger scalar dissipation rates are necessary in the LES-PDF calculations. As observed in the LES calculations in Figure 21, the large, non-physical peak of the scalar dissipation rate at the centerline is present in the LES-PDF calculations as well. This observation gives further reason to work toward improving the numerical and modeling methods in LES.

D. Modeling the molecular and turbulent mixing

The *attenuation of variance production* model as implemented by the *attenuated random walk* described in Sec. V A is assessed next in this flow. This part of the work serves only as an introduction to this type of model and implementation, and does not attempt to exhaustively characterize the performance; rather the focus of this part of the current work is to give some general ideas on how to implement the method, examine some possible definitions for value of β, and to compare the results observed here to the experimental measurements for this one flow.

The first value examined is $\beta = 0.2$. The interpretation of this model is that the production of scalar variance from ν_T is counteracted by a dissipation of 20% of the production. A second investigated value for the model constant is one chosen based on the turbulence resolution scale. Here, the choice of $\beta = \widetilde{\nu}/(\nu_T + \widetilde{\nu})$ is used, although this definition is certainly not unique, nor is it necessarily the best. With this value of β, the DNS limit, where the turbulence is fully resolved, yields no production or dissipation due to ν_T. This property is true anyway, as long as ν_T goes to zero at the DNS limit. Where the turbulence resolution scale is large, β tends toward zero. In practice, the

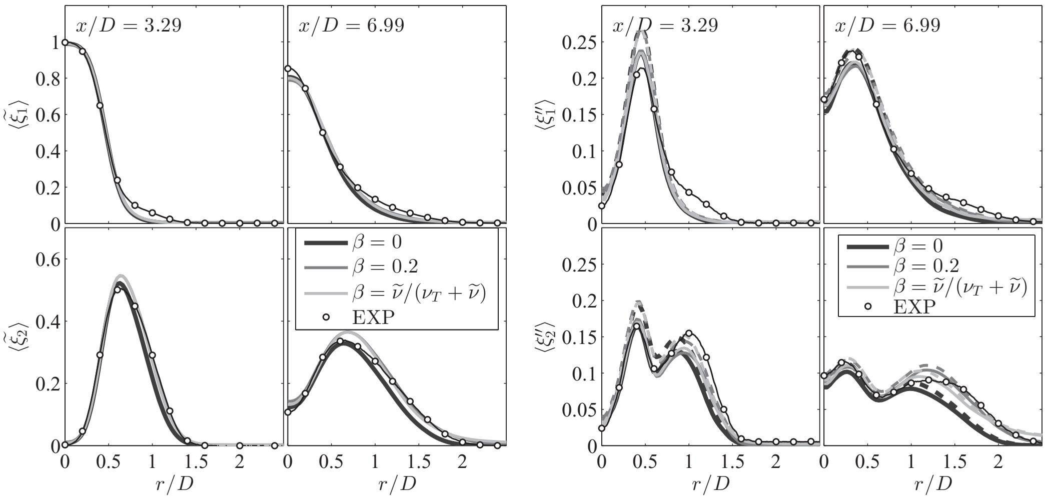

(a) (b)

FIG. 29. Radial profiles of time-averaged mass-weighted mean (a) and RMS (b) mixture fractions in the LES-PDF calculations for different models for β. Black line: $\beta = 0$; dark gray line: $\beta = 0.2$; light gray line: variable β model, $\beta = \widetilde{\nu}/(\nu_T + \widetilde{\nu})$. solid lines: resolved statistics; dashed lines: total statistics; circles: experimental data.[36]

values of $\widetilde{\nu}$ are always greater than zero, and the values of ν_T are always finite, so β is always greater than zero; in other words, there is always some amount of dissipation of variance counteracting the production. The logic in using this type of model contains the underlying assumption that where the turbulence is well-resolved, the conditional diffusion is also well-resolved and there is no dissipation or production of the unresolved variance due to ν_T; where the conditional diffusion is poorly resolved, a small value of β causes the production of the unresolved variance due to ν_T to be large.

Radial profiles of the mean and RMS statistics from LES-PDF calculations with these two models are compared in Figure 29. The calculations are conducted on Grid-A with a value of $C_M = 5$. It is clear from Eqs. (19) and (22)–(23) that the value of β has no direct effect on the mean composition. The small differences that arise in the mean fields, therefore, are due to both the effects of density coupling through the velocity field, and the numerical error in the particle transport. As discussed in Sec. IV C, the LES calculations yield slightly larger values of $\langle\widetilde{\xi_2}\rangle$ than measured experimentally due to the thin-wall modeling assumption. Therefore, the values of $\langle\widetilde{\xi_2}\rangle$ from the two new models are in fact improved from the standard model.

The RMS fields are also affected by the choice of β. The increase in the RMS in the annulus-coflow mixing layer ($1 < r/D$) is attributed mainly to the small changes in the mean in this region. The change in the amount of the RMS which is unresolved (the total minus the resolved) is nearly indiscernible from Figure 29. The expected behavior of a positive value of β is to decrease the amount of unresolved scalar fluctuations. Comparing with Figure 26, the value of β has a much smaller effect on the unresolved fluctuations than does the value of C_M. For these conditions, the dissipation of the modeled variance is dominated by the molecular mixing term.

VI. DISCUSSION

As experimental methodologies continue to advance, much more knowledge of the physical processes involved can be brought to light. It is increasingly important to be able to validate these experimental results, as well as to use the experimental results to validate computational models. This work addresses progress in both of these areas. A recently conducted experiment of a turbulent coaxial jet[36] is studied computationally through RANS-PDF, LES, and LES-PDF methodologies, and many detailed statistics from the calculations and experiments are compared.

Since there is little dependence of density feedback in the flow field (especially compared to reacting flows, where the maximum density varies by a factor as large as ten), this flow presents a good test case for the mixing models. Whereas many previous studies of mixing models in RANS-PDF calculations are conducted in reacting flows,[6,7,17,20] the work performed here is in an inert flow; this fact gives an advantage to the comparisons done in this work because any uncertainties associated with modeling the chemistry are removed.

However, when interpreting these results and applying the conclusions to PDF calculations of reacting flows, one must be mindful of the conditions of this flow. In reacting flows, the temperatures are as much as 2000 K larger than the ambient temperature here; furthermore, many species important to ignition (for example, H, OH, and H_2) are substantially lighter than the species measured in this flow (C_2H_4 and C_3H_6O). As a consequence of both of these facts, the molecular diffusivities of many species important to chemical reaction can be as much as 10–100 times larger than the molecular diffusivities of the species in this flow. So, it is important to realize that in LES-PDF of reacting flows, the contribution of molecular transport for some important species is much larger than what is observed in this work. LES studies have confirmed that molecular diffusion is indeed important in reacting flows, particularly in the near-field of the flow.[59] Given that most of the uncertainties in comparing the conditional diffusion from the calculations and experiments arises from the relatively large turbulent diffusivity, it is expected that reacting flows would yield less of this type of error; this occurs due a larger portion of the total diffusivity being from the molecular diffusivity, particularly at high temperatures and for light species.

The mean and RMS statistics of the flow field can be calculated with very high accuracy using LES, provided the resolution in the LES is sufficient. For the mean fields, sufficient accuracy is achieved when around 20%–40% of the total viscosity is resolved; for the RMS fields, this occurs when around 30%–60% of the total viscosity is resolved. For the quantities of scalar dissipation rate and the conditional diffusion, the LES results provide insight on both the quality of the modeling, and of the interpretation of the experimental results. The LES calculations with resolution even higher than the experimental resolution show that the scalar dissipation rate may not be fully resolved in the experiment, and really ought to be interpreted as a scalar dissipation of the resolved fields. Therefore, when comparing calculations to the experimental measurements, one must keep in the mind the resolution with which both are made. The LES and RANS-PDF modeling of the total scalar dissipation rate suggest a total scalar dissipation rate somewhere between 5 and 10 times larger than the measure resolved scalar dissipation rates. Nevertheless, one must also take into account the quality of the models used to make these estimates. The fact that RANS-PDF and LES models for the scalar dissipation rate have as much as 50% variation between them shows that improvements in models for the scalar dissipation rate would be insightful, and that this flow would be a good test for such models.

The LES-PDF calculations yield encouraging results for this new, developing methodology. The good agreement between the experimental measurements of the joint PDFs and those obtained with LES-PDF calculations is one example of such a result from this study. When one is interested in higher-order statistics of the composition PDF (for example, in the case of pollutant dispersion, where the probability of a certain pollutant to exceed a certain limit must be quantified), LES-PDF calculations are shown here to be an ideal methodology, as they demonstrate a strong capability to reproduce the observed joint PDF of compositions. Conversely, one must be cautious when using RANS-PDF to make calculations of higher-order statistics, as evident in the comparisons of joint PDFs computed in this work. While the RANS-PDF calculations with the MC mixing model yield scalar statistics similar to that of the LES-PDF and the experiment, the RANS-PDF calculations with the IEM and EMST models yield quite different joint scalar PDFs.

When comparing different computational methods, it is critical to account for the computational cost of each method. In this study, the RANS-PDF calculations on Grid-4 (numerical error around 2% for most quantities) required approximately 48 h on 16 CPUs, or a total of 768 CPU hours for one calculation. This time includes both the time to reach a statistically stationary state and the time to sufficiently time-average the statistics. The LES calculations on Grid-B (numerical error around 8% for most quantities) required nearly the same time, around 48 h on 16 CPUs, for a total of 768 CPU hours. For the LES calculations on Grid-D (numerical error around 2% for most quantities), the calculations required approximately 96 h on 64 CPUs, for a total of about 6100 CPU hours. For the LES-PDF calculations on Grid-B, each computation required approximately 72 h on 128 cores, or 9200 CPU hours. While the LES-PDF calculations required the most computational time, they do benefit from having better parallel scalability, since a large part of the particle solver work can be done without any communication.

The *attenuation of variance production* model in LES-PDF introduced here is valuable because it yields an additional dissipation term in the variance transport equation, which is equal to the production times the factor β. The improvement on the coarse grids is encouraging, though it still needs to be better understood. Since the value of β really has little impact on the mean scalar fields, the results indicate that the improvement is actually caused by reduced numerical error in the particle transport using this method. In many previous LES-PDF studies, total RMS statistics of scalars are not reported; when they are reported, they are often overpredicted.[64,67,68] In some cases, improved RMS statistics can be obtained through unreasonably large values of the mixing model constant, C_M.[67] This newly proposed model offers a promising alternative approach to this problem. This work serves only as an introduction to such a model, and more conclusive testing should be done in other flows, the values for β ought to be more thoroughly characterized, and the effects of numerical errors must be better understood.

An important question arising from this work concerns the difference between the conditional diffusion measured experimentally and calculated by LES and LES-PDF. It is observed here that as the LES grid is refined, both the resolved scalar dissipation and resolved conditional diffusion show reasonable agreement with the experimental measurements for similar resolution scales. It is also observed that these statistics are highly dependent on the resolution, and even on the finest LES grid, they show no signs of reaching convergence. A further observation is that the structure of the resolved conditional diffusion in scalar space is relatively similar for all grid sizes, and of a similar form to the structure observed experimentally. It is not until the total conditional diffusion is computed that the structure of the conditional diffusion in scalar space significantly deviates from the experimentally measured form (as evident from Figures 22 and 23). Likewise, the LES-PDF results yield a conditional diffusion which is similar to the total conditional diffusion from the LES calculations.

There are two possible reasons for this difference between the experimental and calculated conditional diffusion: (i) the experimental resolution being too low, and (ii) the modeling of the turbulent diffusivity in LES. This could be tested through DNS of this flow, although the Reynolds number, 14 300 is still somewhat large compared to that of other DNS studies. A second possible way to investigate this is through experiments with a higher imaging resolution, or experiments at a lower Reynolds number, accompanied by DNS study. Through this kind of study, the fully resolved conditional diffusion could be obtained from the DNS and compared to that measured experimentally. The modeling of the turbulent diffusivity is eliminated in this problem, and the effects of the experimental resolution can be explicitly tested by examining the DNS data at the same resolution.

VII. CONCLUSIONS

In summary, this work uses RANS-PDF, LES, and LES-PDF computational methodologies to model a three-stream turbulent coaxial jet studied experimentally in Ref. 36. The major conclusions of this study are as follows:

- RANS-PDF calculations with all mixing models (IEM, MC, and EMST) are capable of yielding mean and RMS fields in good agreement with the experimental measurements; however, the joint PDFs of the two mixture fractions yielded by each model show a wide variability with each other and with the experimental data. Of all the mixing models studied with RANS-PDF, the MC model comes closest to the experimentally measured joint scalar PDFs.
- The EMST mixing model yields a PDF which lies almost exactly on the slow mixing manifold identified in the experimental work, but entirely lacks the fast manifold. This suggests that the slow mixing manifold exists due to aspects of mixing represented by the model (mixing local in composition space), while the fast manifold is due to physical processes and aspects of mixing

which the model does not consider (for example, velocity-conditioned mixing or differential diffusion).
- LES calculations on successively refined grids display excellent convergence toward the experimentally measured mean and RMS fields. The resolution quality of these calculations is carefully assessed. The resolved scalar dissipation rate and resolved conditional diffusion from these calculations are in good agreement with the experimental measurements, but depend strongly on the resolution.
- LES-PDF calculations yield joint PDFs of the mixture fractions in good agreement with the experiments, better than the RANS-PDF calculations with the IEM or EMST mixing models and slightly better than those with the MC mixing model.
- The *attenuation of variance production* model is introduced, implemented through the *attenuated random walk*, and tested in this flow. This model yields an additional dissipation term in the transport equation for scalar variance which counteracts the production caused by the turbulent diffusivity. Results show improved predictions of the mean and RMS fields in LES-PDF on coarse grids, due to reduced numerical error incurred by this model as well as the reduced production of modeled variance.

This work presents a thorough study of a novel multi-stream non-reacting flow using a variety of computational approaches. The behavior of the calculations has been investigated in terms of nontrivial statistics including the scalar dissipation rate and the conditional diffusion. The advances from experimental methodologies given in Ref. 36 has allowed a comparison of these revealing, insightful statistics to actual experimental data, and this work is aimed at using this novel experimental data to assess the quality of the current models and to test new model implementations. Careful work is performed to examine the experimental data of these statistics, and to assess the impact of the resolution at which they are made. The knowledge on multi-scalar mixing can be furthered and models can be refined to predict this physical process with even greater accuracy by (i) working further from the experimental study,[36] (ii) utilizing the findings of this study and other detailed comparisons,[40] (iii) addressing the remaining questions identified in this work on the role of the turbulent diffusivity on the conditional diffusion, and (iv) examining this process in other flow configurations.

ACKNOWLEDGMENTS

The authors extend their thanks to Professor Chenning Tong for providing the experimental data and sharing the details of the experimental work. This work was supported in part by NSF Award No. CBET-1033246. This research was made with government support under and awarded by DoD, Air Force Office of Scientific Research, National Defense Science and Engineering Graduate (NDSEG) Fellowship, 32 CFR 168a. This work used the Extreme Science and Engineering Discovery Environment (XSEDE), which is supported by National Science Foundation (NSF) Grant No. OCI-1053575.

[1] S. B. Pope, “PDF methods for turbulent reactive flows,” Prog. Energy Combust. Sci. **11**, 119 (1985).
[2] D. C. Haworth, “Progress in probability density function methods for turbulent reacting flows,” Prog. Energy Combust. Sci. **36**, 168 (2010).
[3] R. P. Lindstedt, S. A. Louloudi, and E. M. Váos, “Joint scalar probability density function modeling of pollutant formation in piloted turbulent jet diffusion flames with comprehensive chemistry,” Proc. Combust. Inst. **28**, 149 (2000).
[4] J. Xu and S. B. Pope, “PDF calculations of turbulent nonpremixed flames with local extinction,” Combust. Flame **123**, 281 (2000).
[5] R. P. Lindstedt and S. A. Louloudi, “Joint scalar transported probability density function modeling of turbulent methanol jet diffusion flames,” Proc. Combust. Inst. **29**, 2147 (2002).
[6] R. R. Cao, S. B. Pope, and A. R. Masri, “Turbulent lifted flames in a vitiated coflow investigated using joint PDF calculations,” Combust. Flame **142**, 438 (2005).
[7] R. R. Cao, H. Wang, and S. B. Pope, “The effect of mixing models in PDF calculations of piloted jet flames,” Proc. Combust. Inst. **31**, 1543 (2007).
[8] J. Villermaux and J. C. Devillon, “Representation de la coalescence et de la redispersion des domaines de segregation dans un fluide par un modele d’interaction phenomenologique,” in *Proceedings of the Second International Symposium on Chemical Reaction Engineering* (Elsevier, New York, 1972).

[9] C. Dopazo and E. E. O'Brien, "An approach to the autoignition of a turbulent mixture," Acta Astronaut. **1**, 1239 (1974).
[10] R. L. Curl, "Dispersed phase mixing-theory and effects in simple reactors," AIChE J. **9**, 175 (1963).
[11] J. Janicka, W. Kolbe, and W. Kollmann, "Closure of the transport equation for the probability density function of turbulent scalar fields," J. Non-Equilib. Thermodyn. **4**, 47 (1979).
[12] S. Subramaniam and S. B. Pope, "A mixing model for turbulent reactive flows based on Euclidean minimum spanning trees," Combust. Flame **115**, 487 (1998).
[13] D. W. Meyer and P. Jenny, "A mixing model for turbulent flows based on parameterized scalar profiles," Phys. Fluids **18**, 035105 (2006).
[14] D. W. Meyer and P. Jenny, "Micromixing models for turbulent flows," J. Comput. Phys. **228**, 1275 (2009).
[15] D. W. Meyer, "A new particle interaction mixing model for turbulent dispersion and turbulent reactive flows," Phys. Fluids **22**, 035103 (2010).
[16] K. Gkagkas and R. P. Lindstedt, "The impact of reduced chemistry on auto-ignition of H_2 in turbulent flows," Combust. Theory Modell. **13**, 607 (2009).
[17] K. Liu, S. B. Pope, and D. A. Caughey, "Calculations of bluff-body stabilized flames using a joint PDF model with detailed chemistry," Combust. Flame **141**, 89 (2005).
[18] D. Geyer, A. Dreizler, J. Janicka, A. D. Permana, and J. Y. Chen, "Finite-rate chemistry effects in turbulent opposed flows: Comparison of Raman/Rayleigh measurements and Monte Carlo PDF simulations," Proc. Combust. Inst. **30**, 711 (2005).
[19] M. J. Dunn, A. R. Masri, R. W. Bilger, and R. S. Barlow, "Finite rate chemistry effects in highly sheared turbulent premixed flames," Flow Turbul. Combust. **85**, 621–648 (2010).
[20] D. H. Rowinski and S. B. Pope, "PDF calculations of piloted premixed jet flames," Combust. Theory Modell. **15**, 245 (2011).
[21] F. Bisetti, J. Y. Chen, E. R. Hawkes, and J. H. Chen, "Probability density function treatment of turbulence/chemistry interactions during the ignition of a temperature-stratified mixture for application to HCCI engine modeling," Combust. Flame **155**, 571 (2008).
[22] Z. Warhaft and J. L. Lumley, "An experimental study of the decay of temperature fluctuations in grid-generated turbulence," J. Fluid Mech. **88**, 659 (1978).
[23] C. Beguier, I. Dekeyser, and B. E. Launder, "Ratio of scalar and velocity dissipation time scales in shear flow turbulence," Phys. Fluids **21**, 307 (1978).
[24] B. Ma and Z. Warhaft, "Some aspects of the thermal mixing layer in grid turbulence," Phys. Fluids **29**, 3114 (1986).
[25] W. J. A. Dahm and P. E. Dimotakis, "Mixing at large Schmidt number in the self-similar far field of turbulent jets," J. Fluid Mech. **217**, 299 (1990).
[26] D. R. Dowling and P. E. Dimotakis, "Similarity of concentration field of gas-phase turbulent jets," J. Fluid Mech. **218**, 109 (1990).
[27] Jayesh and Z. Warhaft, "Probability distribution, conditional dissipation, and transport of passive temperature fluctuations in grid-generated turbulence," Phys. Fluids A **4**, 2292 (1992).
[28] N. R. Panchapakesan and J. L. Lumley, "Turbulence measurements in axisymmetric jets of air and helium. Part 2. Helium jet," J. Fluid Mech. **246**, 225 (1993).
[29] V. Eswaran and S. B. Pope, "Direct numerical simulations of the turbulent mixing of a passive scalar," Phys. Fluids **31**, 506 (1988).
[30] E. E. O'Brien and T. L. Jiang, "The conditional dissipation rate of an initially binary scalar in homogeneous turbulence," Phys. Fluids A **3**, 3121 (1991).
[31] M. R. Overholt and S. B. Pope, "Direct numerical simulation of a passive scalar with imposed mean gradient in isotropic turbulence," Phys. Fluids **8**, 3128 (1996).
[32] P. K. Yeung, X. Shuyi Xu, and K. R. Sreenivasan, "Schmidt number effects on turbulent transport with uniform mean scalar gradient," Phys. Fluids **14**, 4178 (2002).
[33] P. K. Yeung, D. A. Donzis, and K. R. Sreenivasan, "High-Reynolds-number simulation of turbulent mixing," Phys. Fluids **17**, 081703 (2005).
[34] C. M. Cha, S. M. de Bruyn Kops, and M. Mortensen, "Direct numerical simulations of the double scalar mixing layer. Part I: Passive scalar mixing and dissipation," Phys. Fluids **18**, 067106 (2006).
[35] C. Tong and Z. Warhaft, "Scalar dispersion and mixing in a jet," J. Fluid Mech. **292**, 1 (1995).
[36] J. Cai, M. J. Dinger, W. Li, C. D. Carter, M. D. Ryan, and C. Tong, "Experimental study of three-scalar mixing in a turbulent coaxial jet," J. Fluid Mech. **685**, 495 (2011).
[37] A. Juneja and S. B. Pope, "A DNS study of turbulent mixing of two passive scalars," Phys. Fluids **8**, 2161 (1996).
[38] P. K. Yeung, "Correlations and conditional statistics in differential diffusion: Scalars with uniform mean gradients," Phys. Fluids **10**, 2621 (1998).
[39] B. L. Sawford and S. M. de Bruyn Kops, "Direct numerical simulation and Lagrangian modeling of joint scalar statistics in ternary mixing," Phys. Fluids **20**, 095106 (2008).
[40] D. W. Meyer and R. Deb, "Modeling molecular mixing in a spatially inhomogeneous turbulent flow," Phys. Fluids **24**, 025103 (2012).
[41] S. B. Pope, "On the relationship between stochastic Lagrangian models of turbulence and second-moment closures," Phys. Fluids **6**, 973 (1994).
[42] R. O. Fox, "On velocity-conditioned scalar mixing in homogeneous turbulence," Phys. Fluids **8**, 2678 (1996).
[43] S. B. Pope, "The vanishing effect of molecular diffusivity on turbulent dispersion: Implications for turbulent mixing and the scalar flux," J. Fluid Mech. **359**, 299 (1998).
[44] S. B. Pope, *Turbulent Flows* (Cambridge University Press, Cambridge, 2000).
[45] D. C. Haworth and S. B. Pope, "A generalized Langevin model for turbulent flows," Phys. Fluids **29**, 387 (1986).
[46] P. R. Van Slooten, Jayesh, and S. B. Pope, "Advances in PDF modeling for inhomogeneous turbulent flows," Phys. Fluids **10**, 246 (1998).

[47] M. Muradoglu, S. B. Pope, and D. A. Caughey, "The hybrid method for the PDF equations of turbulent reactive flows: Consistency conditions and correction algorithms," J. Comput. Phys. **172**, 841 (2001).

[48] B. E. Launder, G. J. Reece, and W. Rodi, "Progress in the development of a Reynolds-stress turbulence closure," J. Fluid Mech. **68**, 537 (1975).

[49] M. M. Gibson and B. E. Launder, "Ground effects on pressure fluctuations in the atmospheric boundary layer," J. Fluid Mech. **86**, 491 (1978).

[50] S. B. Pope, "Self-conditioned fields for large-eddy simulations of turbulent flows," J. Fluid Mech. **652**, 139 (2010).

[51] C. D. Pierce and P. Moin, "Progress-variable approach for large-eddy simulation of non-premixed turbulent combustion," J. Fluid Mech. **504**, 73 (2004).

[52] P. Domingo, L. Vervisch, and D. Veynante, "Large eddy simulation of a lifted jet flame in a vitiated coflow," Combust. Flame **152**, 415 (2008).

[53] K. A. Kemenov, H. Wang, and S. B. Pope, "Modeling effects of subgrid-scale mixture fraction variance in LES of a piloted diffusion flame," Combust. Theory Modell. **16**, 611 (2012).

[54] M. Germano, U. Piomelli, P. Moin, and W. H. Cabot, "A dynamic subgrid-scale eddy viscosity model," Phys. Fluids A **3**, 1760 (1991).

[55] D. K. Lilly, "A proposed modification of the Germano subgrid-scale closure method," Phys. Fluids A **4**, 633 (1992).

[56] A. W. Vreman, "An eddy-viscosity subgrid-scale model for turbulent shear flow: Algebraic theory and applications," Phys. Fluids **16**, 3670 (2004).

[57] H. Pitsch and H. Steiner, "Large-eddy simulation of a turbulent piloted methane/air diffusion flame (Sandia flame D)," Phys. Fluids **12**, 2541 (2000).

[58] M. Ihme and H. Pitsch, "Prediction of extinction and reignition in nonpremixed turbulent flames using a flamelet/progress variable model: 2. Application in LES of Sandia flames D and E," Combust. Flame **155**, 90 (2008).

[59] K. A. Kemenov and S. B. Pope, "Molecular diffusion effects in LES of a piloted methane-air flame," Combust. Flame **158**, 240 (2011).

[60] H. Wang, P. P. Popov, and S. B. Pope, "Weak second-order splitting schemes for Lagrangian Monte Carlo particle methods for the composition PDF/FDF transport equations," J. Comput. Phys. **229**, 1852 (2010).

[61] R. McDermott and S. B. Pope, "A particle formulation for treating differential diffusion in filtered density function methods," J. Comput. Phys. **226**, 947 (2007).

[62] S. Viswanathan, H. Wang, and S. B. Pope, "Numerical implementation of mixing and molecular transport in LES/PDF studies of turbulent reacting flows," J. Comput. Phys. **230**, 6916 (2011).

[63] H. Wang and S. B. Pope, "Large eddy simulation/probability density function modeling of a turbulent $CH_4/H_2/N_2$ jet flame," Proc. Combust. Inst. **33**, 1319 (2011).

[64] H. Wang, M. Juddoo, S. H. Starner, A. R. Masri, and S. B. Pope, "A novel transient turbulent jet flame for studying turbulent combustion," Proc. Combust. Inst. **34**, 1251 (2013).

[65] Y. Yang, H. Wang, S. B. Pope, and J. H. Chen, "Large-eddy simulation/probability density function modeling of a nonpremixed CO/H_2 temporally evolving jet flame," Proc. Combust. Inst. **34**, 1241 (2013).

[66] H. Pitsch, "Large-eddy simulation of turbulent combustion," Annu. Rev. Fluid Mech. **38**, 453 (2006).

[67] D. H. Rowinski and S. B. Pope, "Computational study of lean premixed turbulent jet flames using RANS-PDF and LES-PDF methods," Combust. Theory Modell. **17**, 610 (2013).

[68] M. R. H. Sheikhi, T. G. Drozda, P. Givi, F. A. Jaberi, and S. B. Pope, "Large eddy simulation of a turbulent nonpremixed piloted methane jet flame (Sandia Flame D)," Proc. Combust. Inst. **30**, 549 (2005).